Dynamical Signatures of Trumpler 19: A Statistical and Photometric Perspective

A. H. Sheikh[1] ⓘ, Biman J. Medhi[1] ⓘ, and Ram Sagar[2] ⓘ

[1] Department of Physics, Gauhati University, Guwahati 781014, Assam, India; asheikh@gauhati.ac.in
[2] Indian Institute of Astrophysics, Block II, Koramangala, Bangalore 560034, India

Abstract

We present a statistical approach to investigating the dynamical evolution of the old open cluster Trumpler 19. We identified 810 cluster members using an ensemble-based unsupervised machine learning method applied to Gaia Data Release 3 astrometric data. From the color–magnitude diagram, we identified 18 blue straggler stars (BSSs) in Trumpler 19. The mass function of the cluster shows a flatter slope, indicating strong mass segregation and advanced dynamical evolution. We fitted the radial surface density profile and found that the concentration parameter $c > 1$, suggesting that the cluster has formed a clear core–halo structure as a result of dynamical evolution. We characterized the mass segregation among the cluster members as well as BSSs using the Minimum Spanning Trees method, indicating a significant central concentration. Additionally, the sedimentation level of the BSSs is measured as $A_{rh}^{+} = 0.28 \pm 0.05$, further supporting radial segregation. To probe the BSS formation mechanisms, we estimated their fractional mass excess (M_e), supporting binary mass transfer and mergers as the dominant channels. This is further supported by the presence of six variable BSSs. The dynamical evolution of the cluster is further assessed through its tidal interaction with the Galaxy. Trumpler 19 appears to be within the tidal regime, where strong Galactic tidal forces have a significant influence on the dynamical evolution. This indicates that the cluster may have undergone significant mass-loss processes, potentially leading to its eventual disruption, which is further supported by the orbit analysis of the cluster. We found that Trumpler 19 may have lost more than 95% of its initial mass due to dynamical evolution.

Unified Astronomy Thesaurus concepts: Astronomy data analysis (1858); Open star clusters (1160); Hertzsprung Russell diagram (725); Blue straggler stars (168); Stellar astronomy (1583); Stellar dynamics (1596)

1. Introduction

Old open clusters are regarded as important tools for investigating stellar evolution and the dynamics of stellar systems. These clusters offer a unique perspective on the effects of stellar evolution, gravitational interactions, and mass loss over extended periods. The process of mass loss is primarily driven by internal dynamics, where interactions between stars play a key role (G. Meylan & D. C. Heggie 1997; H. J. G. L. M. Lamers et al. 2010). The mechanism responsible for this is called two-body relaxation, which occurs when stars in the system interact gravitationally with each other (E. Vesperini 2010). These interactions gradually lead to a redistribution of energy among the stars, driving the system toward energy equipartition, where stars of different masses begin to settle into more stable configurations (P. Bianchini et al. 2016). Over time, this process results in mass segregation, where more massive stars tend to move toward the center, while lower-mass stars are pushed to the outskirts. This internal evolution leads to the gradual loss of stars, especially lighter ones, from the outer regions of the cluster, contributing to its mass loss (E. Khalisi et al. 2007). In addition to internal dynamics, external factors also play a significant role in shaping the evolution of open clusters. The Galactic potential can cause tidal interactions that strip stars from the cluster (R. Elson et al. 1987). Tidal shocks, which are abrupt disturbances caused by the cluster passing through regions of higher gravitational potential (such as near the galactic disk or spiral arms), can also lead to the loss of stars

(H. Baumgardt & J. Makino 2003). These external factors, combined with internal dynamics, significantly influence the long-term evolution and survival of open clusters.

These processes significantly influence the stellar populations typically observed in star clusters, including main-sequence (MS) stars, main-sequence turnoff (MSTO) stars, and red giant branch (RGB) stars, and also play a key role in the evolution of binary stars, leading to the formation of unusual and exotic populations (K. K. Rao et al. 2023). One such group is blue straggler stars (BSSs), which are peculiar massive stars in a cluster. These stars are thought to form through binary or higher-order stellar interactions, such as mass transfer, mergers, or stellar collisions (W. H. McCrea 1964; H. B. Perets & D. C. Fabrycky 2009; N. Leigh et al. 2011; S. Chatterjee et al. 2013). In the Hertzsprung–Russell (H-R) diagram, BSSs are distinct, as they appear both brighter and bluer than the MSTO point (A. R. Sandage 1953). This is particularly intriguing, because the MSTO represents the stage at which stars of similar mass and age transition off the MS. Since all stars in a cluster are generally formed at nearly the same time, stars above the MS are not expected (A. H. Sheikh & B. J. Medhi 2024a, 2024b). In addition to their unique position on the H-R diagram, BSSs tend to be more centrally concentrated within clusters compared to other stellar populations (M. J. Rain et al. 2021). Their higher mass relative to other stars in the cluster makes them subject to mass segregation, where they migrate toward the cluster core over time. BSSs are excellent probes of cluster dynamics, due to their unique formation mechanisms and distinctive properties. By studying their spatial distribution, kinematics, and evolutionary status, we can trace energy redistribution processes, test theoretical models of cluster

dynamics, and understand the impacts of internal and external forces on cluster evolution.

The interplay of physical processes driving cluster dissolution and morphology remains debated. N-body simulations by R. de La Fuente Marcos (1997) and E. Terlevich (1987) showed that cluster evolution is influenced by the initial mass function (IMF), stellar mass loss, primordial binaries, and tidal interactions, highlighting mass segregation driven by low-mass star escape. Analytical models of H. J. G. L. M. Lamers et al. (2005a, 2005b), based on outcomes from H. Baumgardt & J. Makino (2003) and GALEV models (J. Schulz et al. 2002; P. Anders & U. Fritze-v. Alvensleben 2003), accurately described cluster mass loss, aligning well with simulations. The dynamical evolution of open clusters has been extensively analyzed using Gaia data. K. K. Rao et al. (2021, 2023) estimated the sedimentation level (A_{rh}^{+}) for several open clusters using various stellar populations, finding weak correlations with other dynamical age markers and classifying open clusters into three dynamical stages based on their A_{rh}^{+} and N_{relax}, the ratio of the cluster age to the central relaxation time. Similarly, M. S. Angelo et al. (2021, 2023) demonstrated that internal relaxation leads to increased central concentration and reduced susceptibility to tidal disruption, with structural parameters like the core radius (r_c), tidal radius (r_t), half-mass radius (r_h), half-light radius (r_l), and Jacobi radius (r_J) varying with dynamical age and Galactic position. J. Maurya et al. (2023) quantified mass segregation using the Minimum Spanning Trees (MST) method, linking mass segregation and tidal interaction effects to cluster structure, with r_h/r_t positively correlated with Galactocentric distance.

The remaining of the paper is organized as follows: In Section 2, we describe the selected target cluster. Section 3 details the archival data sources used for the analysis. Section 4 presents the determination of the cluster membership probabilities using ensemble-based unsupervised machine learning techniques. Section 5 contains the statistical and photometric analysis, which is used to estimate the fundamental parameters, identify BSSs, determine the MFs, and estimate the structural parameters. In Section 6, we discuss the BSS formation mechanism and variable BSSs. Subsequently, the dynamical evolution of the cluster, including mass segregation, orbit analysis, tidal filling, and cluster mass loss, are discussed in Section 7. The results obtained from these studies and comparisons with previous studies are discussed in Section 8.

2. Target Selection

The investigation of BSSs in old open clusters is of high interest, because they provide critical insights into cluster dynamics and the role of binary systems in cluster evolution. BSSs are extensively studied in globular clusters, but a systematic analysis with reliable membership confirmation is still lacking for open clusters (A. H. Sheikh & B. J. Medhi 2024a). Old open clusters, with their relatively uniform stellar populations and well-determined ages, offer an ideal environment for studying BSS formation mechanisms and their dynamical effects. So, we selected a less-studied cluster, Trumpler 19, to investigate the dynamical state of the cluster, including BSS formation. Trumpler 19—R.A. (α) = 168.°623, decl. (δ) = −57.°563 and Galactic longitude (l) = 290.°195, Galactic latitude (b) = +02.°891—is an old open cluster having an age ∼4 Gyr, [Fe/H] ∼ −0.015, and located

at a distance of ∼2.51 Kpc (N. V. Kharchenko et al. 2013; W. S. Dias et al. 2021). Trumpler 19 is situated in the inner Galactic disk, approximately 7.84 Kpc from the Galactic center and at a vertical distance of ∼ 146 pc from the Galactic plane (T. Cantat-Gaudin & F. Anders 2020; Y. Tarricq et al. 2021).

3. Archival Data

In our study, we used data from Gaia Data Release 3 (DR3; Gaia Collaboration et al. 2023). Gaia DR3 is an essential resource, providing detailed astrometric and photometric information for more than 1.4 billion stars (L. Lindegren et al. 2021). This data set includes precise measurements of star positions (α, δ), parallaxes (π), and proper motions ($\mu_\alpha \cos \delta$, μ_δ), with radial velocity (RV) data available for a subset of stars. It also provides brightness measurements in three photometric bands: G, G_{BP}, and G_{RP}. The catalog covers a wide range of star brightnesses, from very bright stars at $G = 3$ mag to fainter ones down to $G = 21$ mag. One of the key improvements in Gaia DR3 is the significant reduction of systematic errors in its astrometric data. For stars brighter than $G = 15$, parallax uncertainties are as low as 0.02–0.03 mas, while for the faintest stars $G = 21$, these uncertainties rise to about 1.3 mas. Similarly, proper-motion uncertainties are just 0.02–0.03 mas yr^{-1} for brighter stars but can reach 1.4 mas yr^{-1} for the faintest stars.

4. Cluster Membership Analysis

The availability of Gaia DR3 data has greatly improved our ability to identify reliable cluster members, by providing highly accurate measurements of proper motions, parallaxes, and RVs. Recent studies have applied a wide range of machine learning methods—such as ANN, DBSCAN, HDBSCAN, KMEANS, k-nearest neighbor (kNN), Gaussian Mixture Model (GMM), RANDOMFOREST, and UPMASK—to analyze multidimensional astrometric data and distinguish cluster stars from field stars. While these techniques have been successful, they also come with challenges, such as the risk of underfitting or overfitting when working with complex multi-dimensional data sets (M. Agarwal et al. 2021; A. H. Sheikh et al. 2025).

To overcome these issues, we used an unsupervised ensemble machine learning approach. Specifically, we applied a GMM with two components to the one-dimensional Gaussian distribution of Mahalanobis distances (MDs) for the stars. This method minimizes the chances of underfitting or overfitting compared to more traditional multidimensional techniques, providing a more reliable way to identify cluster members (S. Deb et al. 2022). This technique involves the following two main steps.

4.1. kNN Technique for Outlier Removal

In the first step of our analysis, we applied the kNN algorithm to select a relevant range of astrometric parameters —parallax (π), proper motion in R.A. ($\mu_\alpha \cos \delta$), and proper motion in decl. (μ_δ)—for stars within a $5'$–$10'$ search radius. This range is expected to contain more cluster stars than field stars. The kNN algorithm (T. Cover & P. Hart 1967) is used to identify and eliminate probable outliers (field stars) based on the average nearest neighbor distance ($\bar{d}_{NN}$). This value is calculated as the mean Euclidean distance between a star and
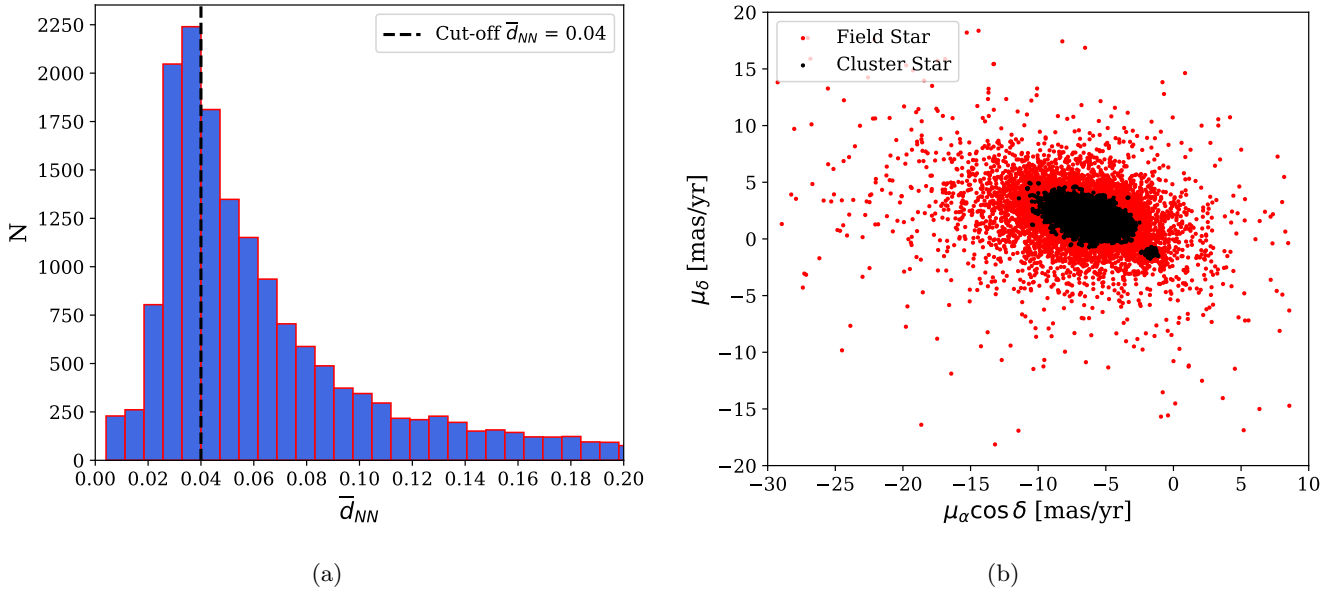
(a)

(b)

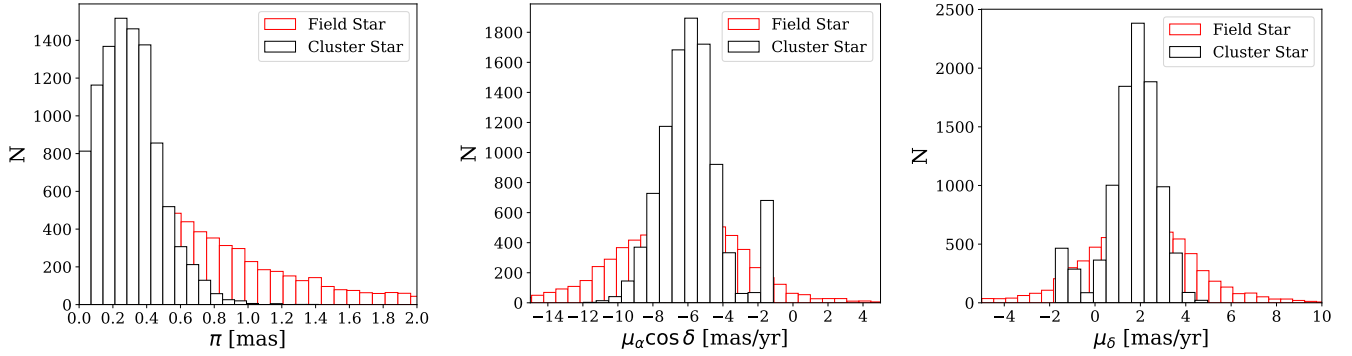**Figure 1.** (a) The distributions of $\bar{d}_{NN}$ for Trumpler 19. (b) The distributions of proper motions for Trumpler 19.

Figure 2. The distributions of π, $\mu_\alpha\cos\delta$, and μ_δ of cluster stars (black) for Trumpler 19 are shown in the left, middle, and right panels, respectively.

its closest neighbors in a three-dimensional parameter space of (π, $\mu_\alpha \cos \delta$, μ_δ; S. Deb et al. 2022; A. H. Sheikh & B. J. Medhi 2024c). Stars with $\bar{d}_{NN}$ greater than a threshold value (t) are considered outliers. The value of t is chosen to be relatively small for $\bar{d}_{NN}$, to ensure a significant predominance of cluster stars over field stars (A. H. Sheikh et al. 2025). The $\bar{d}_{NN}$ is calculated using the equation

$$\bar{d}_{NN} = \sum_k \frac{d(x, k)}{NN_k}, \tag{1}$$

where $d(i, k)$ is the Euclidean distance between the ith star and its kth nearest neighbor, and NN_k is the total number of nearest neighbors. We applied this technique to the astrometric data for Trumpler 19 with a parallax criterion of $\pi \geqslant 0$. The resulting $\bar{d}_{NN}$ distribution and the proper-motion plot are shown in Figures 1(a) and (b), respectively. We used $k = 5$ nearest neighbors, as this offered a clear separation between cluster and field stars while reducing the misclassification of core members. The outlier threshold $t = 0.04$ was chosen based on the inflection point in the $\bar{d}_{NN}$ distribution, where field contamination increases. There is no fixed rule for setting this threshold; we selected it based on visual inspection and its consistency with the proper-motion and parallax density distributions, where values beyond this indicate scattered field

Table 1
Selected Range of Parameters: Parallax (π) and Two Proper Motions ($\mu_\alpha\cos\delta$ and μ_δ) for Trumpler 19

Radius (arcmin)	Cutoff $\bar{d}_{NN}$	π (mas)	$\mu_\alpha \cos \delta$ (mas yr^{-1})	μ_δ (mas yr^{-1})
10	0.04	[0.0, 1.0]	[−2.5, −1.0]	[−2.0, −0.5]

populations. The parameter distributions are shown in Figure 2 and the range of astrometric parameters are listed in Table 1. These distributions exhibit distinct peaks, aiding in identifying cluster stars. This filtering step is essential for identifying true cluster members and removing many field stars, which helps in narrowing the analysis for open cluster membership for stars within a larger search radius using GMM (A. H. Sheikh et al. 2025).

4.2. GMM on MD Distribution

A GMM with two components is applied to the one-dimensional distribution of the MD (P. C. Mahalanobis 1927; P. Mahalanobis 1936), derived from the astrometric parameters—parallax (π) and proper motions ($\mu_\alpha \cos \delta$, μ_δ)—of stars within a larger search radius. The MD, which measures how far a point lies from the mean of a multivariate
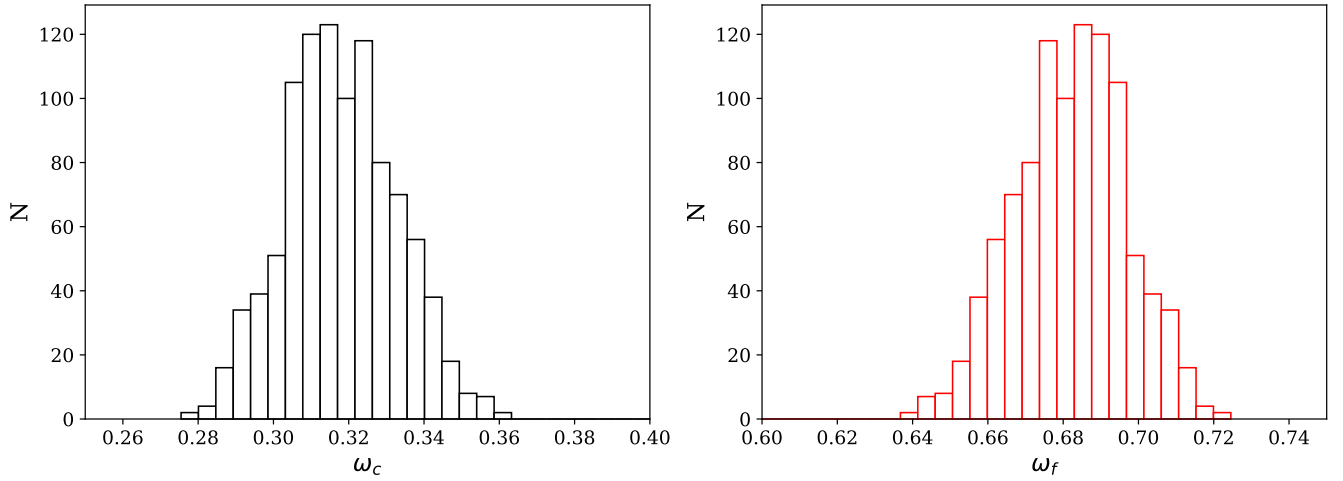
Figure 3. The distributions of the GMM component weights from 1000 bootstrap realizations for the cluster stars (left) and field stars (right), respectively.

distribution in standard deviation units, is calculated after normalizing the data using the covariance matrix (S. Deb et al. 2022). This step ensures comparability across variables, by standardizing the data and removing correlations (A. H. Sheikh et al. 2025).

The MD distribution is then analyzed using a two-component GMM with the Expectation–Maximization (EM) algorithm, which models the data as a combination of two Gaussian distributions: one for cluster stars and another for field stars (G. J. McLachlan & D. Peel 2000; W. H. Press et al. 2007; M. P. Deisenroth et al. 2020). Each component is parameterized by weights, means, and variances (w_c, μ_c, and σ_c) for cluster stars and (w_f, μ_f, and σ_f) for field stars, respectively, and the overall probability density is given by

$$P(D_M|\mu, \sigma^2) = w_c P_c(D_M|\mu_c, \sigma_c^2) + w_f P_f(D_M|\mu_f, \sigma_f^2) \quad (2)$$

and

$$w_c + w_f = 1, \quad (3)$$

where D_M is the MD for a data point $\boldsymbol{x} = (x_1, x_2, \ldots, x_n)$ from a data set with a mean $\boldsymbol{\mu} = (\mu_1, \mu_2, \ldots, \mu_n)$ and covariance matrix and is given by the equation

$$D_M(\boldsymbol{x}) = \sqrt{(x - \mu)^T \Sigma^{-1}(x - \mu)}. \quad (4)$$

The EM algorithm refines the initial parameter estimates, and the membership probabilities, r_{ic}, are calculated as

$$r_{ic} = \frac{w_c P_c(D_{M,i}|\mu_c, \sigma_c^2)}{w_k P_k(D_{M,i}|\mu_k, \sigma_k^2)}. \quad (5)$$

To reduce the arbitrariness in selecting the membership probability threshold, we used bootstrap-based resampling of the MD distribution. We generated 1000 bootstrap samples and fitted a two-component GMM to each. For each realization, we recorded the weights of the cluster and field components (w_c and w_f) and computed the membership probabilities for the original data set. We analyzed the distribution of w_c and w_f across all bootstrap samples, which were found to be stable, indicating the robustness of the GMM-based classification, as shown in Figure 3. To evaluate the sensitivity of the membership count to the choice of probability thresholds, ranging from 0.2 to 0.9, and to compute the number of stars classified as members across all bootstrap

realizations, an optimal threshold is determined, by minimizing the relative variability in member counts. This yielded an optimal threshold of $r_{ic} = 0.54$, as shown in Figure 4(a). The membership probability distribution is shown in Figure 4(b). The one-dimensional MD distribution reveals distinct peaks for cluster and field stars, simplifying visualization and reducing the risks of under- or overfitting compared to higher-dimensional methods. We obtained astrometric data for the parallax (π) and proper motions ($\mu_\alpha \cos \delta$, μ_δ) of Trumpler 19 using a parallax criterion of $\pi \geqslant 0$. To refine these data, we applied parameter ranges determined by the kNN technique and then used them to compute the MD in the parameter space of (π, $\mu_\alpha \cos \delta$, μ_δ). The MD distributions for Trumpler 19 are illustrated in Figure 5(a).

We used a GMM with two components to analyze the MD distributions. The GMM fits for the cluster, field, and combined components are shown in Figure 5(a). By applying a cluster membership probability threshold of >0.54, we identified 810 stars as members of Trumpler 19. The Gaussian fits to the distributions of the astrometric parameters provide the mean values of parallax (π) and proper motions ($\mu_\alpha \cos \delta$, μ_δ), which are listed in Table 2. The color–magnitude diagram (CMD) for the cluster members is shown in Figure 6. Figure 5(b) illustrates the proper-motion directions ($\mu_\alpha \cos \delta$, μ_δ) of these cluster stars, mapped to their respective positions on the sky (α, δ), with the colors representing membership probabilities. Interestingly, most cluster members exhibit uniform motion in the same direction, indicating the reliability and precision of our cluster membership determination.

5. Statistical and Photometric Analysis

5.1. Estimation of Astrophysical Parameters

The (G_{BP}–G_{RP}) versus G CMD for the cluster members of Trumpler 19 is shown in Figure 6. In the CMD, we can clearly see a well-defined MS with a distinct TO point.

To accurately estimate the fundamental astrophysical parameters of age, distance, metallicity, and extinction for Trumpler 19, we adopted a Bayesian approach, using Markov Chain Monte Carlo (MCMC) sampling. This method fits MIST isochrones based on the MESA stellar evolution models (T. D. Morton 2015; J. Choi et al. 2016) to the observed CMD, ensuring statistical reliability in the results. For each set of parameters, a synthetic isochrone is generated, and random
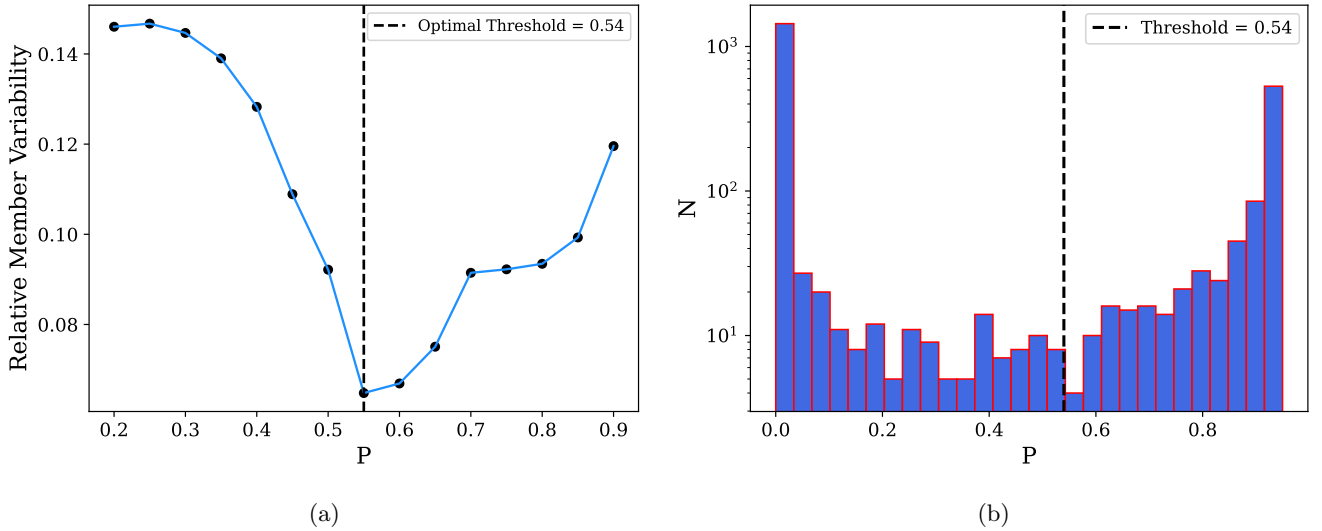
(a)   (b)

Figure 4. (a) The relative variability of the number of members as a function of probability. (b) The distribution of membership probabilities assigned by the GMM model.
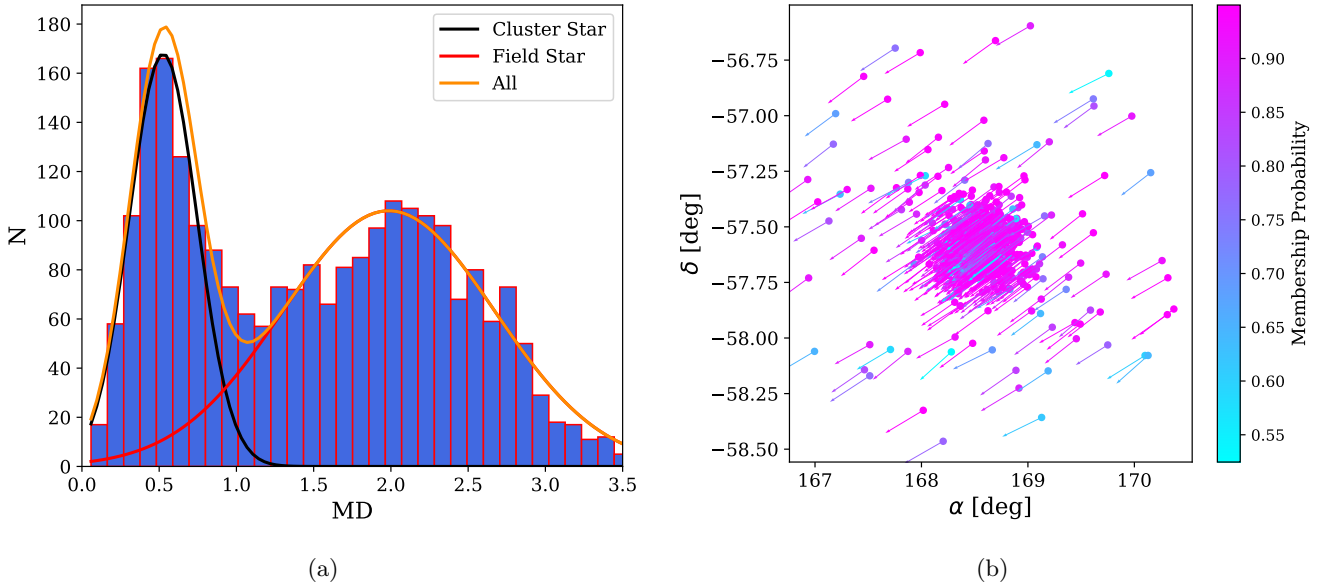

(a)   (b)

Figure 5. (a) The MD distributions for Trumpler 19, modeled using the two-component GMM, and the resulting fits for the cluster (black line), field stars (red line), and both of them together (orange line). (b) The proper-motion vector plot for the cluster members illustrates the uniform direction of motion among member stars relative to their positions in the sky, with each star color-coded according to its membership probability.

photometric errors based on observed photometric uncertainties are added to simulate observational scatter. To ensure a fair comparison, both synthetic and observed CMDs are confined to the same color and magnitude limits, then transformed into two-dimensional histograms over color–magnitude space, using uniform binning and normalization to yield probability density distributions. We measure the agreement between the observed and synthetic CMDs using the Poisson likelihood ratio from M. Tremmel et al. (2013).

The MCMC sampling is carried out using the EMCEE Python package (D. Foreman-Mackey et al. 2013), employing 200 parallel walkers over 2000 iterations, with an initial burn-in of 200 steps, to ensure convergence. We evaluated the Gelman–Rubin statistic ($\hat{R}$) for all estimated astrophysical parameters and found $\hat{R} = 1.03$, which indicates good convergence of the MCMC chains. The best-fitted

astrophysical parameters obtained from this method are listed in Table 3. The best-fitted isochrone for Trumpler 19 is shown in Figure 6 by the black dashed line. The black solid line denotes the zero-age main sequence (ZAMS). The posterior distributions of the parameters are shown in Figure 7. The blue solid line indicates the sample median value (50th percentile), representing the best-fit parameter value. The magenta dashed lines correspond to the upper (84th percentile) and lower (16th percentile) uncertainty bounds.

5.2. Identification of BSSs

We used a well-defined method to identify the BSSs in star clusters. These stars are unusual, because they are brighter and bluer than typical stars at the MSTO on the CMD. To identify potential BSSs, we apply the criteria defined by M. J. Rain et al. (2021), focusing on the region in the CMD where BSSs

Table 2
Obtained Mean Values of the Astrometric Parameters: Parallax (π) and Two Proper Motions ($\mu_\alpha \cos \delta$ and μ_δ)

Radius (arcmin)	No. of Cluster Members	π (mas)	$\mu_\alpha \cos \delta$ (mas yr^{-1})	μ_δ (mas yr^{-1})
60	810	0.396 ± 0.003	-1.672 ± 0.005	-1.216 ± 0.004

are typically found. A BSS is characterized by its position on the CMD, where it is both bluer and brighter than the MSTO point, which is close to or on the ZAMS of the cluster (M. J. Rain et al. 2020). We also define the expected locations of equal-mass binaries by shifting the isochrone upward by 0.752 mag (M. J. Rain et al. 2020; A. H. Sheikh & B. J. Medhi 2024b). This adjustment reflects the maximum brightness for binaries made up of normal stars at the MSTO, helping us identify regions where these binaries would be found (M. J. Rain et al. 2021; A. H. Sheikh & B. J. Medhi 2024a). Using these criteria, we identify 18 BSSs in Trumpler 19, shown in Figure 6 as the blue open circles.

5.3. Estimation of MF

The MF is defined as the distribution of masses within a population of stars. Since the properties and evolution of a star are intimately linked to its mass, the stellar MF is an important tool for studying the evolution of stellar populations (A. H. Sheikh & B. J. Medhi 2024c). By comparing the present-day MF with the IMF, we can trace evolutionary changes over time.

To estimate the individual stellar masses in a cluster, we generate synthetic clusters using theoretical isochrones and sample 10,000 stars following the Chabrier and Salpeter IMFs (E. E. Salpeter 1955; G. Chabrier 2003). Photometric errors are added based on Gaia uncertainties (Gaia Collaboration et al. 2016). Each observed star is matched to its closest synthetic counterpart by minimizing the Euclidean distance in multiband magnitude space (A. Almeida et al. 2023; A. H. Sheikh et al. 2025), which is given by

$$d_i = \min_{s \in S} \sqrt{\sum_{j=1}^{m} (O_{ij} - S_{sj})^2}, \qquad (6)$$

where d_i is the minimum distance between an observed star in an observed cluster O and the sth star in the synthetic cluster S, calculated over m photometric bands, where O_{ij} and S_{sj} represent the magnitudes in the jth band. The synthetic star with the smallest distance is considered the best match, and its mass is assigned to the observed star.

Characterization of the binary fraction is essential, as binaries, whether primordial or formed through later dynamical processes, have a notable influence on the stellar MF (A. H. Sheikh & B. J. Medhi 2024c). Including binary stars in the analysis results in a flatter MF slope (R. Sagar & T. Richtler 1991). This is because unresolved binaries, if ignored, are mistaken for single, more massive stars, leading to an overestimation of high-mass stars and an underestimation of low-mass stars. By properly accounting for binaries, we recover the contribution of low-mass companions and correct the system masses, producing a more accurate and flatter MF. However, identifying binaries is still challenging when data are limited, especially in crowded or distant clusters, where spatial resolution and RV measurements are insufficient. This

limitation can introduce biases into mass estimates and binary fraction determination. Each observed star is matched to a synthetic star, with binary systems included. If the matched synthetic star is a binary, both primary and secondary masses are assigned; otherwise, only the single-star mass is used. The binary population is modeled assuming a power-law dependence of the form $f(q) \propto q^\gamma$, where $q = M_{\text{sec}}/M_{\text{prim}} \leqslant 1$ is the mass ratio between the secondary and primary components of a binary. Additionally, the likelihood of a star being in a binary system is defined as a function of its primary mass, using the equation

$$P_B(M_{\text{prim}}) = \alpha + \beta \times \frac{M_{\text{prim}}}{1.4 + M_{\text{prim}}}. \qquad (7)$$

In this model, $P_B(M_{\text{prim}})$ gives the probability of binary membership for a star of mass M_{prim}, with α and β acting as free parameters that shape the binary fraction distribution across stellar masses. We adopt $\alpha = 0.09$ and $\beta = 0.94$, consistent with a very reasonable fit to the observed multiplicity distribution (S. S. R. Offner et al. 2023), leading to an estimated binary fraction of $f_B \approx 0.66$ and a power-law index of $\gamma \approx 0.47$ for Trumpler 19.

To ensure statistical robustness, this procedure is repeated several times, by generating new synthetic clusters through the stochastic variation of stellar properties (A. Almeida et al. 2023). The final stellar mass assigned to each observed star is the median of all estimated values, while the uncertainty is computed as the standard deviation of the mass distribution. A two-part segmented linear MF is defined as

$$f(x) = \begin{cases} \alpha_B x + b_1, & \text{for } M \leqslant M_C \\ \alpha_A x + b_2, & \text{for } M > M_C \end{cases}, \qquad (8)$$

where α_A is the slope for high masses and α_B that for low masses, transitioning at a characteristic mass M_C. Intercepts b_1 and b_2 are adjusted to ensure continuity at M_C. To estimate the total cluster mass, the mean binary mass ratio is derived from observed binaries and applied to primary stars following the observed MF. Using the binary fraction f_B, the total mass is then calculated:

$$M_T = M_O + M_{un}(1 + f_B \times q), \qquad (9)$$

where M_T is the total mass, M_O is the mass from observed stars, and M_{un} is the mass from the MF integration over unobserved stars.

We generated the synthetic cluster using the best-fitted astrophysical parameters for Trumpler 19 and then estimated the stellar masses using the Monte Carlo method.[3] Figure 8 shows the distribution of different stellar masses for the member stars of Trumpler 19. The MF is fitted to the histogram of the mass distribution, with the number of bins

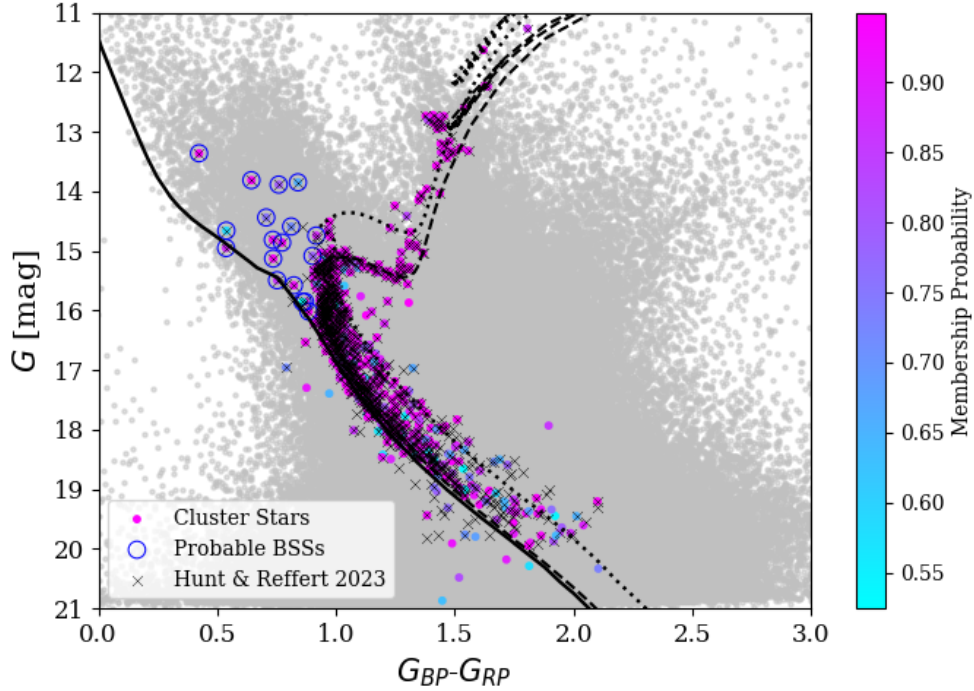---

[3] https://github.com/ander-son-almeida/DashboardOCmass

Figure 6. The CMD for the member stars of Trumpler 19. The black solid line represents the ZAMS. The black dashed line is the best-fitted isochrone. The black dotted line shows the equal-mass binary locus. The black "x" represents the cluster members from E. L. Hunt & S. Reffert (2023).

Table 3
The Estimated Best-fitted Astrophysical Parameters for Trumpler 19

Age (Gyr)	Distance (Kpc)	[Fe/H]	A_v (mag)
3.71 ± 0.29	2.37 ± 0.03	-0.05 ± 0.12	0.77 ± 0.07

determined using the rule set by H. A. Sturges (1926). The upper panel of figure 9 shows the fitted MF slope (blue solid line) for single stars, while the lower panel presents the MF slope accounting for binary populations. Since the power-law distribution does not extend to the lowest stellar masses ($M < 0.4\,M_\odot$; E. E. Salpeter 1955; P. Kroupa 2001; G. Chabrier 2003), we performed least-squares fitting for stars with mass $M > 0.4\,M_\odot$. The MF slope for single stars is determined to be $\alpha_A = -1.22 \pm 0.11$ in the high-mass range and $\alpha_B = 4.11 \pm 0.17$ in the low-mass range. When binary systems are taken into account, the MF slopes become $\alpha_A = -0.92 \pm 0.08$ for the high-mass end and $\alpha_B = 3.99 \pm 0.21$ for the low-mass end. In both cases, the transition mass between the two regimes is found to be $0.91\,M_\odot$. The total mass of the cluster obtained for Trumpler 19 is $2398 \pm 123\,M_\odot$ and the mean mass is $0.87 \pm 0.02\,M_\odot$. In the case of Trumpler 19, the obtained MF slopes are flatter than the E. E. Salpeter (1955) value ($\alpha = -1.35$) for solar neighborhood conditions, indicating a deficiency of low-mass stars and suggesting that the cluster has undergone significant dynamical evolution. This suggests Trumpler 19 has experienced significant dynamical evolution, typical of dissolving open clusters, where low-mass stars are lost through mass segregation and external perturbations such as two-body relaxation, interactions with giant molecular clouds (GMCs), encounters, and Galactic tidal effects.
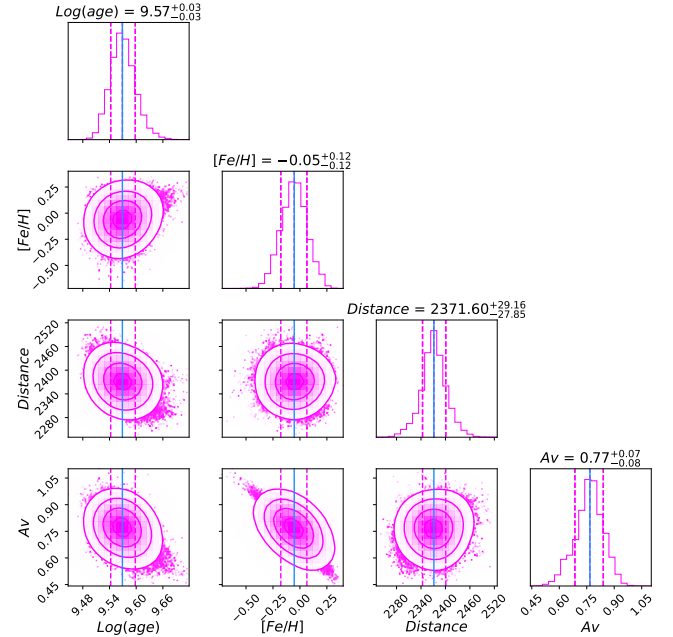

Figure 7. Posterior distributions of the estimated parameters from isochrone fitting for Trumpler 19. The blue solid line represents the median value (50th percentile), indicating the best-fit parameter. The magenta dashed lines mark the uncertainty range, corresponding to the 16th and 84th percentiles.

However, it is important to note that observational limitations may also contribute to this apparent flattening. The incomplete detection of faint low-mass stars, especially in crowded regions or near the detection limit, can bias the derived MF, mimicking or exaggerating the effects of dynamical evolution. This fundamental limitation is particularly critical for old sparse clusters, where low-mass members
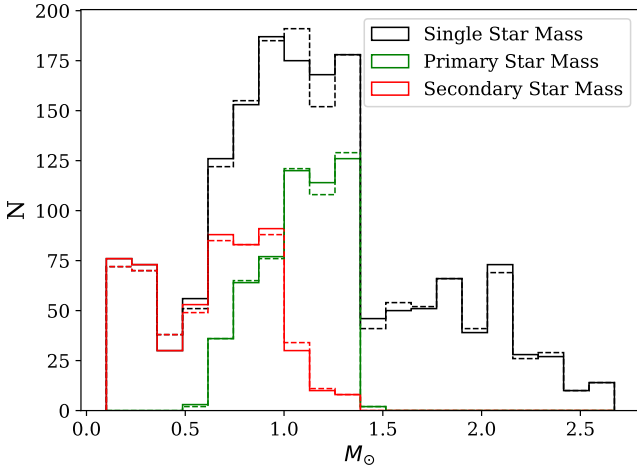
Figure 8. The distribution of stellar masses for member stars of Trumpler 19, showing single stars in black, primary components in green, and secondary components in red. The solid lines represent the masses derived from the G. Chabrier (2003) IMF and the dashed lines represent the masses from the E. E. Salpeter (1955) IMF.

are both intrinsically faint and more likely to have been lost or missed observationally.

5.4. Estimation of Structural Parameters

The radial surface density profile is a crucial tool for analyzing the spatial distributions of stellar populations in open clusters, helping to define their size and structure in the celestial coordinate plane (α–δ; S. Deb et al. 2022; A. H. Sheikh & B. J. Medhi 2024c). This profile reveals how stellar density changes with distance from the cluster center, aiding in understanding cluster dynamics, mass segregation, and evolutionary history (A. H. Sheikh & B. J. Medhi 2024a, 2024b). The radial surface density profile can be fitted using an I. King (1962) fit, given as (R. Carrera et al. 2019; Y. Tarricq et al. 2022)

$$\rho(r) = \rho_0 \left(\frac{1}{\sqrt{1 + \left(\frac{r}{r_c}\right)^2}} - \frac{1}{\sqrt{1 + \left(\frac{r_t}{r_c}\right)^2}} \right)^2 + \rho_{bg}, \quad (10)$$

where ρ_0 is the core density, r_c is the core radius (where $\rho = \rho_0/2$), r_t is the tidal radius (where $\rho = \rho_{bg}$), and ρ_{bg} is the background density. The radial distance r of the ith star from the center of the cluster (α_0–δ_0) is calculated as

$$\cos r = \cos \delta_i \cos \delta_0 \cos(\alpha_i - \alpha_0) + \sin \delta_i \sin \delta_0. \quad (11)$$

The stellar surface density ρ_i is estimated as $\rho_i = N_i/A_i$, where N_i is the number of stars in the ith ring and $A_i = \pi(r_{i+1}^2 - r_i^2)$ is the ring area. Density uncertainties follow Poisson statistics: $\sigma_{pi} = \sqrt{N_i}/A_i$ (Y. Tarricq et al. 2022). For Trumpler 19, the radial profiles are fitted using Bayesian MCMC sampling with the EMCEE Python package (D. Foreman-Mackey et al. 2013). The best-fit model and uncertainties are determined using 2000 walkers, 1000 iterations, and 200 burn-in steps (S. Deb et al. 2022; A. H. Sheikh & B. J. Medhi 2024a). The observed data (black dots), best-fit line (red line), and uncertainties (error bars) are shown in Figure 10(a). Additionally, 300 random sample fits generated from the MCMC chains are represented by the blue
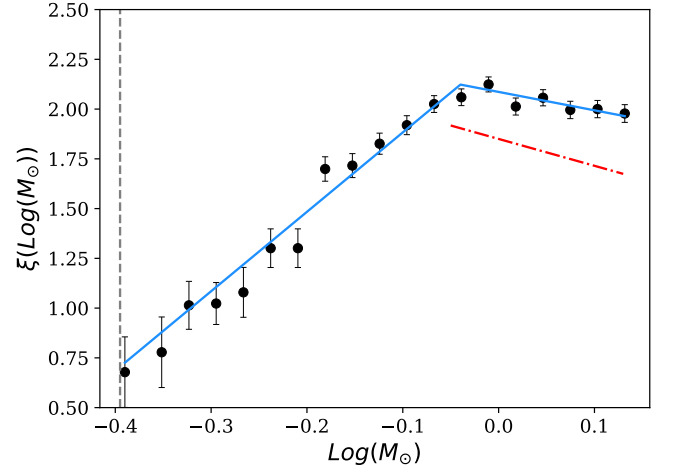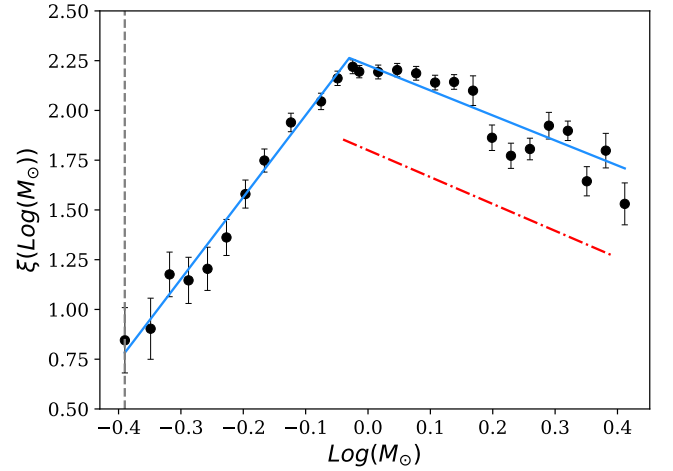

Figure 9. The MF slopes for Trumpler 19 are shown for single stars (top panel) and for binary populations (bottom panel). The blue solid lines represent the MF slopes derived for Trumpler 19, while the red dashed line shows the E. E. Salpeter (1955) IMF, for comparison. The gray dashed lines represent the 0.4 $M_\odot$ cut.

lines, giving us a visual representation of the uncertainties associated with the model parameters (S. Deb et al. 2022; A. H. Sheikh et al. 2025). The marginalized posterior distributions for each parameter from the MCMC chains are illustrated in Figure 10(b). We evaluated the Gelman–Rubin statistic ($\hat{R}$) for all estimated structural parameters and found $\hat{R} = 1.02$, which indicates good convergence of the MCMC chains. The resultant structural parameters for Trumpler 19 are listed in Table 4.

The concentration parameter, defined as $c = \mathrm{Log}(r_t/r_c)$ (C. J. Peterson & I. R. King 1975), quantifies the density profile of a cluster and serves as a key indicator of its internal structure and evolutionary history. This parameter reflects the effects of formation processes, dynamical evolution, and environmental influences on the cluster. For Trumpler 19, $c > 1$ indicates a high degree of central concentration. A high concentration parameter indicates that the cluster has experienced considerable dynamical evolution, resulting in a denser core and a more spread-out halo (A. H. Sheikh & B. J. Medhi 2024b). This suggests that the core radius is much smaller than the tidal radius, signifying a very dense core. Such a condition is typically observed in clusters that have undergone significant dynamical changes, including mass
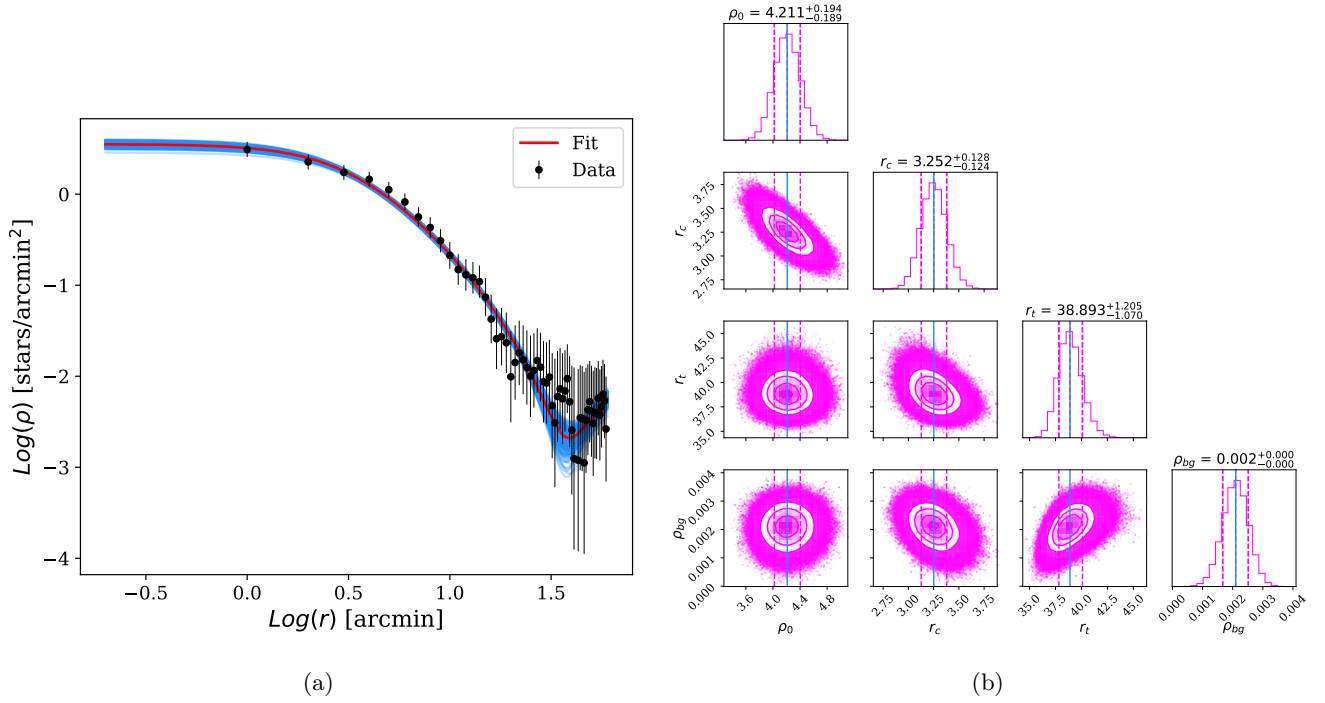
Figure 10. (a) The radial density profile fit for the cluster members of Trumpler 19. (b) The marginalized posterior distributions and uncertainties related to the model parameters of the King profile fit for the cluster members of Trumpler 19.

Table 4
The Estimated Structural Parameters—Core Density (ρ_0), Core Radius (r_c), Tidal Radius (r_t), and Background Density (ρ_{bg})—Using MCMC Analysis

Center (deg)	ρ_0 (stars arcmin^{-2})	r_c (arcmin)	r_t (arcmin)	ρ_{bg} (stars arcmin^{-2})
168.623, −57.563	4.211 ± 0.193	3.251 ± 0.127	38.885 ± 1.156	0.002 ± 0.000

segregation. As more massive stars move toward the center, they increase the central density of the cluster, leading to a higher concentration parameter.

6. BSS Formation Mechanism

Understanding the formation of BSSs in a cluster is closely tied to their mass and the position of the TO point in the CMD. BSSs are thought to have acquired additional mass during their MS lifetime, which can provide insights into their formation pathways. Clues to the potential formation pathways of BSS formation are offered by the most massive stars in the cluster at the time they form. By estimating the excess mass that BSSs have gained, we can infer their formation mechanisms. For this, we used fractional mass excess (M_e), which is defined as (V. V. Jadhav & A. Subramaniam 2021)

$$M_e = \frac{M_{BSS} - M_{TO}}{M_{TO}}, \tag{12}$$

where M_{BSS} is the mass of the BSS and M_{TO} is the cluster TO mass. M_e represents the efficiency of the mass transfer in the case where both the accretor and the progenitor are MSTO stars, which can serve as a proxy for distinguishing between different formation scenarios for BSSs (V. V. Jadhav & A. Subramaniam 2021). By estimating the excess mass that BSSs have gained, we can infer their formation mechanisms. We can categorize BSSs roughly into mergers and mass

transfer products based on the M_e: low-M_e BSSs involve less-efficient mass transfer binaries and mergers with a low-mass secondary, while high-M_e BSSs are primarily the result of conservative mass transfer, indicative of merger-dominated scenarios; extreme-M_e BSSs, exceeding the mass of two MSTO stars, suggest either earlier formation, when MSTO masses were higher, or the merging of more than two MSTO stars (V. V. Jadhav & A. Subramaniam 2021).

We estimated the masses of the BSSs using the Monte Carlo method, by comparing the G magnitudes of the BSSs to the ZAMS, assuming that the BSSs are single stars. Although this mass estimation method has some errors, due to the imperfect alignment between isochrones and the cluster CMD, these errors do not significantly affect the hierarchy of masses within the cluster. We also estimate the mass of the MSTO, $M_{TO} \approx 1.25\,M_\odot$, for Trumpler 19. We find that in Trumpler 19, 10 BSSs have $M_e < 0.5$, indicating they likely gained mass through binary mass transfer; five BSSs have $0.5 < M_e < 1$, suggesting they gained mass through mergers; and three BSSs have $M_e > 1.0$, indicating a likely origin from multiple mergers or mass transfer events.

Now, variable BSSs often suggest ongoing or past mass transfer in binaries, offering insights into binary evolution processes such as Roche-lobe overflow, common-envelope phases, and mass transfer dynamics (A. H. Sheikh & B. J. Medhi 2024a). We searched for the light curves (LCs) in the TESS GSFC-ELEANOR-LITE data releases for these
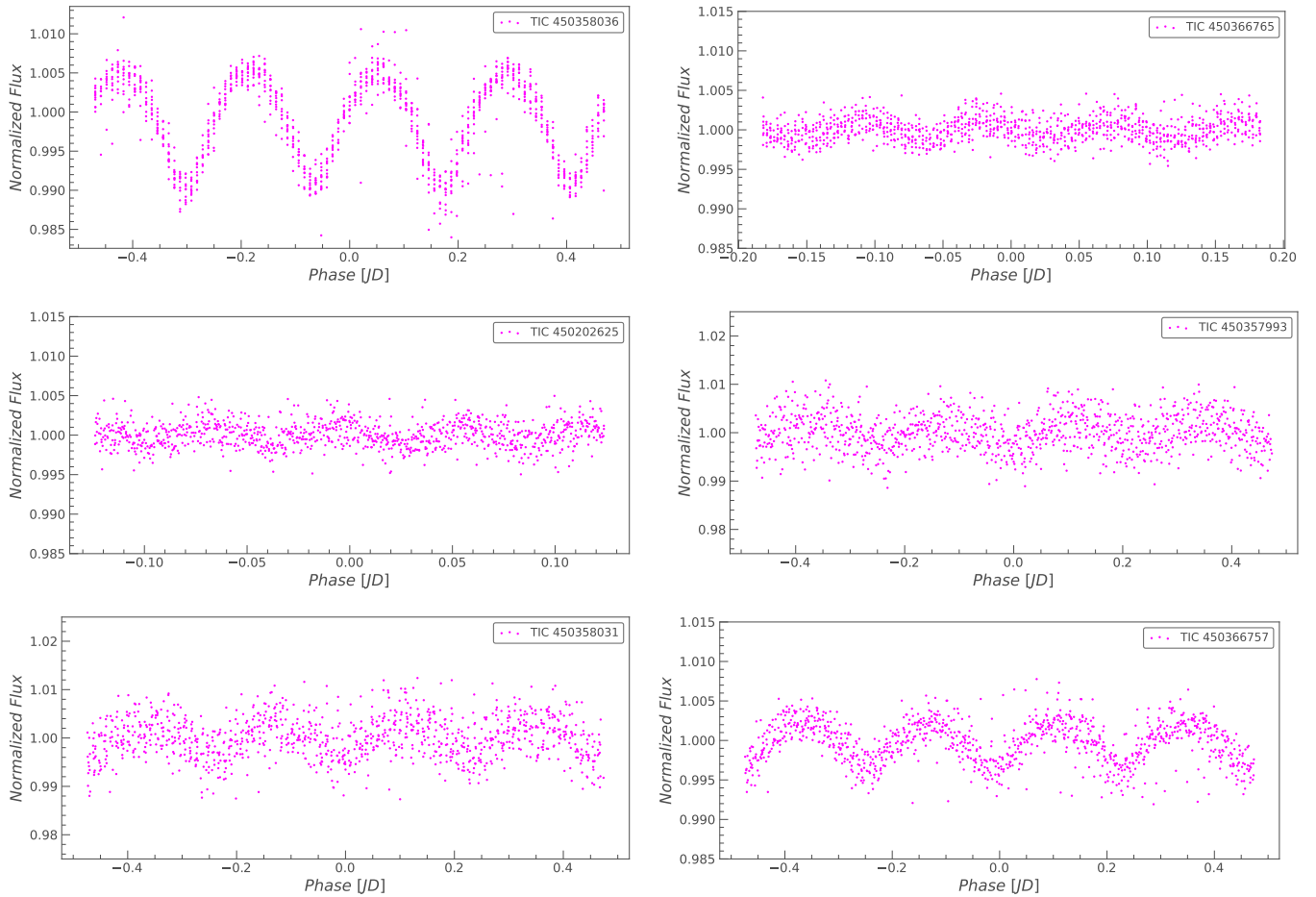
Figure 11. The phase-folded LCs of six BSSs using the period determined in the Lomb–Scargle periodogram.

BSS candidates (B. P. Powell et al. 2022). We found that six BSS candidates showed signs of variability in sector 10 of the TESS data. To construct and analyze the LCs of these six BSSs, we used the Python-based package Lightkurve (Lightkurve Collaboration et al. 2018). The Lomb–Scargle periodogram (W. H. Press & G. B. Rybicki 1989) is used to determine the periodicity and extract all significant frequencies. A frequency is considered significant if its amplitude or power exceeds four times the local noise level (M. Breger et al. 1993). After identifying the relevant frequencies, the orbital frequency typically yields a phase-folded LC with two distinct dips, corresponding to eclipses, whereas other frequencies produce sinusoidal variations, as shown in Figure 11.

It is noteworthy that all six BSSs have a very short orbital period, ranging from 0.12 to 0.47 days. From the LCs of these BSSs, we can say that these BSSs exhibit the characteristics of an eclipsing binary (β Persei (Algol) or β Lyrae type). Such a short period for the eclipsing binary systems suggests that these BSSs may have formed through the mass transfer channel. As massive stars concentrate toward the cluster center, due to mass segregation, binaries containing massive components are also concentrated there. The higher central density increases the probability of binary interactions, making mass transfer more frequent. In such dense cores, the probability of stellar collisions and mergers also rises. BSSs formed via binary mass transfer and mergers are expected to be centrally located in mass-segregated clusters. Therefore, in

Trumpler 19, binary mass transfer and mergers are likely the dominant BSS formation channels.

7. Dynamical Evolution of the Cluster

7.1. Mass Segregation in Trumpler 19

Mass segregation describes the tendency for the more massive stars in a cluster to move toward the center, while lower-mass stars disperse outward. This occurs due to gravitational interactions among stars or as a result of the star formation process (S. Biswas et al. 2024; A. H. Sheikh & B. J. Medhi 2024b, 2024c). Although clusters may initially lack mass segregation, they develop over time, as substructures merge and gravitational forces act on the stars (D. Guszejnov et al. 2022). Evidence of mass segregation is observed in some open clusters, where massive stars are concentrated at the center (H. Sung et al. 2013, 2017; S. Dib & T. Henning 2019). The most massive stars, such as BSSs, experience dynamical friction, causing them to lose momentum and gradually migrate toward the core (A. H. Sheikh & B. J. Medhi 2024b). This results in their concentration near the cluster center.

We investigated the effects of mass segregation among BSSs and cluster members of Trumpler 19 using the radial cumulative distribution function (RCDF; X.-h. Gao 2019; S. Biswas et al. 2024; A. H. Sheikh & B. J. Medhi 2024b), as shown in Figure 12. A two-sided Kolmogorov–Smirnov test is used to evaluate the statistical significance of the differences
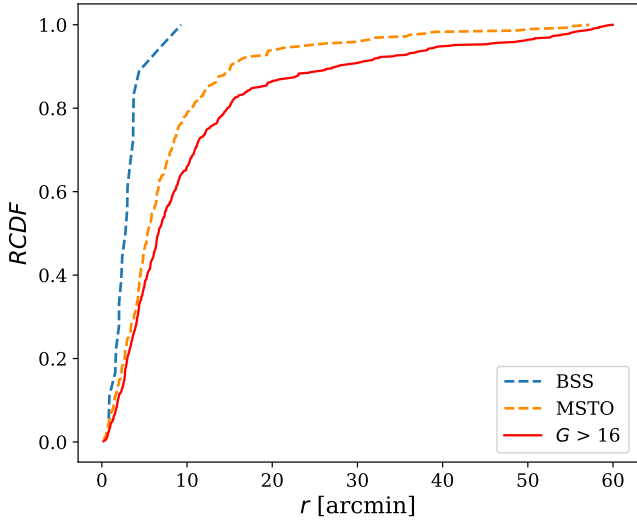
Figure 12. The RCDF for BSSs (blue line), RGBs (orange line), and fainter/low-mass stars with $G > 16$ (red line) for Trumpler 19.

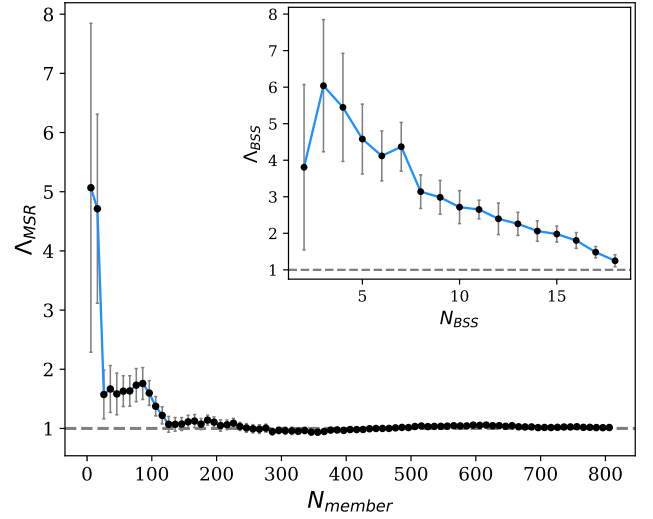**Figure 13.** The Λ_{MSR} vs. N_{member} profile for all the cluster members of Trumpler 19. The inset shows the segregation ratio for BSSs Λ_{BSS} as a function of N_{member}. The gray dashed lines represent no segregation, i.e., $\Lambda_{\mathrm{BSS}} = 1$.

among stellar types. The results indicate that BSSs are more concentrated toward the center than the reference (lighter) MSTO stars, with a significance of 99.99% (p–value = 0.00004) for Trumpler 19. These findings strongly support the presence of mass segregation in the cluster, particularly among the BSSs. The mass segregation in Trumpler 19 likely results from the dynamical evolution. For Trumpler 19, all of the BSSs extend to a radial distance of approximately $9\overset{\prime}{.}31$ ($2.8r_c$). This suggests that BSSs are concentrated in the central region and radially segregated. The higher density of massive stars in the cluster core increases the likelihood of binary interactions, making the mass transfer and mergers more frequent in these regions (A. H. Sheikh & B. J. Medhi 2024b).

Now, to characterize the mass segregation in the cluster for all cluster members and among the BSSs, we used the MST method (R. C. Prim 1957). The MST of a data set is the shortest possible path that connects all points without forming a closed loop (R. C. Prim 1957). A more compact or segregated data set will exhibit a shorter MST length (J. Maurya et al. 2023). We select 810 cluster members and then an equal number of random reference stars. The degree of segregation for cluster members (Λ_{MST}) is calculated as the ratio of the mean MST lengths of random reference stars (L_{random}) to the MST lengths of cluster members (L_{member}) and is given by (R. J. Allison et al. 2009)

$$\Lambda_{\mathrm{MSR}} = \frac{\langle L_{\mathrm{random}} \pm \sigma_{\mathrm{random}} \rangle}{L_{\mathrm{member}}}, \qquad (13)$$

where σ_{random} is the standard deviation of L_{random}. The associated errors in Λ_{MSR} are obtained by repeating this process for 1000 iterations. In the same way, we also characterize the mass segregation among the BSSs. We can say that there is significant mass segregation present in the cluster and the BSSs in Trumpler 19 also exhibit moderate signatures of mass segregation, as shown in Figure 13.

To study the dynamical state and determine the sedimentation level of BSSs, we used the A_{rh}^{+} parameter, the area enclosed between the cumulative radial distributions of BSSs (ϕ_{BSS}) and reference MSTO stars (ϕ_{Ref}; E. Alessandrini et al.

2016). The A_{rh}^{+} parameter is given by the equation

$$A_{rh}^{+} = \int_{x_{\min}}^{x} \phi_{BSS}(x') - \phi_{\mathrm{Ref}}(x')dx', \qquad (14)$$

where $x = \mathrm{Log}(r/r_h)$ and $x_{\min}$ are the outermost and innermost radii from the cluster center, respectively, and r_h is the half-mass radius of the cluster. This dimensionless observational parameter serves as a reliable empirical indicator of the degree of segregation of the BSSs, with its value increasing as the BSSs become more concentrated toward the cluster center (K. K. Rao et al. 2021). A_{rh}^{+} is strongly correlated with the ratio of the cluster age to its current central relaxation time, making it a useful tool for empirically determining the dynamical age of a cluster (B. Lanzoni et al. 2016). The different stellar populations in a cluster are affected to varying extents by the strength of the Galactic field. As a result, the inner regions of a cluster are less influenced by the Galactic field and are more prone to mass segregation driven by two-body relaxation (K. K. Rao et al. 2023). So, we estimated the A_{rh}^{+} parameter up to r_h for Trumpler 19, as shown in Figure 14. We found A_{rh}^{+} to be 0.28 ± 0.05 for Trumpler 19. The errors in the A_{rh}^{+} values are calculated using the bootstrap method, iterating the A_{rh}^{+} estimation 1000 times by resampling the BSSs and reference sample (B. Efron & R. Tibshirani 1993). This also indicates a moderate level of BSS concentration toward the cluster center.

7.2. Dynamical State of Trumpler 19

Dynamical relaxation in a star cluster is the process whereby gravitational interactions among its stars gradually balance out their motions (L. Spitzer 1987). When a cluster forms, its stars have random velocities, but over time, gravitational encounters cause some stars to gain energy and move outward, while others lose energy and sink inward. This reshuffling leads to a more balanced and uniform distribution of velocities. Eventually, the cluster reaches a state of equilibrium, where the energy is more evenly distributed, and the stars settle into stable positions and motions (A. H. Sheikh &
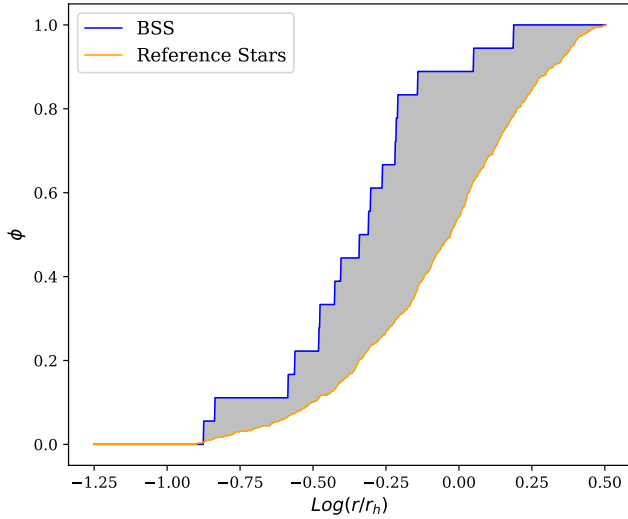
Figure 14. The RCDF of the BSSs (blue line) and reference stars (yellow), plotted against the logarithm of the radial distance from the cluster center (in units of half-mass radius) for Trumpler 19. The values of $A_{r_h}^+$ correspond to the gray shaded area between the RCDF of the BSSs and reference stars.

B. J. Medhi 2024b). The timescale within which a cluster will completely lose any trace of its initial conditions is effectively represented by the relaxation time (t_r) and is given by (L. J. Spitzer & M. H. Hart 1971)

$$t_r = \frac{8.9 \times 10^5 \sqrt{N} \times r_h^{3/2}}{\sqrt{\overline{m}} \times \mathrm{Log}(0.4N)}, \qquad (15)$$

where N represents the number of cluster members, r_h is the half-mass radius in parsecs, and $\overline{m}$ is the average mass of the cluster stars. The half-mass radius, r_h, is defined as the radius within which half of the total cluster mass is enclosed and can be expressed by the equation

$$r_h = 0.547 \times r_c \times \left(\frac{r_t}{r_c}\right)^{0.486}. \qquad (16)$$

We calculate the value of r_h as $6'.06 \pm 0'.21$ (4.25 ± 0.15 pc) for Trumpler 19. The value of the relaxation time, t_r, is obtained as 96 ± 2 Myr for Trumpler 19. We define the dynamical evolution parameter $\tau = \mathrm{Age}/t_r$, which is found to be $\tau \gg 1$ for Trumpler 19. This indicates that Trumpler 19 is dynamically relaxed. A higher value of τ signifies that the cluster has existed for a significantly longer period relative to its relaxation time, suggesting it has undergone numerous gravitational interactions among its stars and moved closer to a state of equilibrium (A. H. Sheikh & B. J. Medhi 2024a, 2024b). This is supported by the moderate core contraction observed ($r_c/r_h = 0.54$), consistent with internal dynamical evolution driven by two-body relaxation and mass segregation, though the cluster has not yet reached core collapse (M. S. Angelo et al. 2023).

Out of the 810 identified cluster members, 49 stars have RV measurements available from Gaia. To estimate the mean RV and uncertainty of the cluster, we adopted a weighted mean approach, where the RV of each star contributes according to the inverse square of its measurement uncertainty. We found that for Trumpler 19, the mean RV $\bar{v}_{\mathrm{rad}} = -26.86 \pm 0.153 \, \mathrm{km \, s^{-1}}$. Figure 15 shows the RVs of stars as a function of their radial distance from the center of Trumpler 19. Each point includes an
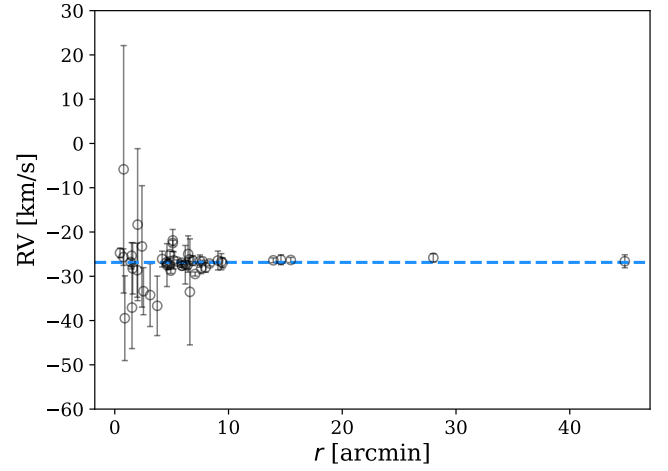

Figure 15. The RVs as a function of the radial distance to the cluster center. The blue dashed line represents the mean RV of the cluster.

error bar representing the uncertainty in the RV measurement. A linear fit to the RV as a function of radial distance yielded an insignificant slope ($0.029 \pm 0.155 \, \mathrm{km \, s^{-1} \, arcmin^{-1}}$, $p = 0.85$), suggesting no clear radial gradient. Additionally, a rotation model based on position angle yielded a modest rotation amplitude of $v_{\mathrm{rot}} = -0.64 \pm 0.17 \, \mathrm{km \, s^{-1}}$ with a position angle of $\theta_0 = 19 \overset{\circ}{.}8 \pm 4\overset{\circ}{.}06$. While these results hint at weak rotational signatures, the limited number of RV measurements and their spatial distribution limit our ability to draw strong conclusions. Therefore, we cautiously interpret Trumpler 19 as dynamically relaxed, although deeper spectroscopic coverage would be required to confirm the absence of rotational motion.

7.3. Orbit Analysis of Trumpler 19

Open clusters are key to understanding Galactic structure and stellar dynamics. Studying their kinematics helps trace their birth radii and spatial distribution, offering insights into star formation and evolution in the Milky Way (A. H. Sheikh & B. J. Medhi 2024c; A. H. Sheikh et al. 2025). We used the MWPotential2014 model from the Galactic dynamics library GALPY[4] (J. Bovy 2015) for the orbit analysis of Trumpler 19, which includes bulge, disk, and halo components of the gravitational potential for the Milky Way. The bulge is modeled using a spherical power-law density profile with an exponential cutoff, as described by J. Bovy (2015):

$$\rho(r) = A\left(\frac{r}{r_1}\right)^{\alpha} \exp\left[-\left(\frac{r}{r_c}\right)^2\right], \qquad (17)$$

where r_1 is a reference radius, r_c is the cutoff radius, A is a normalization constant related to the mass density, and α is the inner slope of the power law. The disk potential for the galactic disk component is proposed by M. Miyamoto & R. Nagai (1975):

$$\Phi_{\mathrm{disk}}(R_{\mathrm{GC}}, Z) = -\frac{GM_d}{\sqrt{R_{\mathrm{GC}}^2 + (a_d + \sqrt{Z^2 + b_d^2})^2}}, \qquad (18)$$

where R_{GC} is the Galactocentric radius, Z is the vertical distance from the Galactic plane, G the gravitational

---

constant, M_d is the mass of the disk, a_d is the radial scale length, and b_d is the vertical scale height. The halo component is given by J. F. Navarro et al. (1996):

$$\Phi_{\text{halo}}(r) = -\frac{GM_s}{R_{\text{GC}}} \ln\left(1 + \frac{R_{\text{GC}}}{r_s}\right), \qquad (19)$$

where M_s is the scale mass of the dark matter halo and r_s is the scale radius. To model nonaxisymmetric features of the Milky Way, we included the rotating central bar and spiral arms, using the DehnenBarPotential and SpiralArmsPotential models. The Dehnen bar potential is given by W. Dehnen (2000):

$$\Phi_{\text{bar}}(R, z, \phi) = A_b(t)\cos\left[2(\phi - \Omega_b t)\right]\left(\frac{R}{r}\right)^2$$

$$\times \begin{cases} -\left(\frac{R_b}{r}\right)^3, & r \geqslant R_b \\ \left(\frac{r}{R_b}\right)^3 - 2, & r < R_b \end{cases}, \qquad (20)$$

where $r = \sqrt{R^2 + z^2}$, Ω_b is the bar pattern speed, and R_b is the bar radius. The time-dependent amplitude $A_b(t)$ evolves as

$$A_b(t) = \begin{cases} 0, & t < t_{\text{form}} \\ A_f\left(\begin{array}{c} \frac{3}{16}\xi^5 - \frac{5}{8}\xi^3 \\ +\frac{15}{16}\xi + \frac{1}{2} \end{array}\right), & t_{\text{form}} \leqslant t \leqslant t_{\text{form}} + t_{\text{steady}}, \\ A_f, & t > t_{\text{form}} + t_{\text{steady}} \end{cases}$$

$$(21)$$

where $\xi = 2(t - t_{\text{form}})/t_{\text{steady}} - 1$. The bar strength parameter is

$$\alpha = \frac{3A_f r_0^3}{v_0^2 R_b^3}, \qquad (22)$$

with r_0 and v_0 being the reference radius and circular velocity. The spiral arm potential is given by D. P. Cox & G. C. Gómez (2002):

$$\Phi_{\text{spiral}}(R, \phi, z) = -4\pi GH\rho_0 \exp\left(-\frac{R - r_{\text{ref}}}{R_s}\right)$$

$$\times \sum_n C_n K_n D_n \cos(n\gamma) \operatorname{sech}^{B_n}(K_n z B_n), \qquad (23)$$

where the spiral phase is

$$\gamma = N\left[\phi - \phi_{\text{ref}} - \frac{\ln(R/r_{\text{ref}})}{\tan\alpha}\right] \qquad (24)$$

and the wave parameters are

$$K_n = \frac{nN}{R\sin\alpha}, \qquad (25)$$

$$B_n = K_n H, \qquad (26)$$

$$D_n = \frac{1 + K_n H + 0.3(K_n H)^2}{1 + 0.3K_n H}. \qquad (27)$$

We adopt a simple sinusoidal spiral pattern by setting $C_n = [1]$.

We carried out the orbital integration of Trumpler 19 using its central coordinates ($\alpha = 168°.623$, $\delta = -57°.563$), mean proper motions ($\mu_\alpha \cos\delta = -1.672 \pm 0.005$ mas yr^{-1}, $\mu_\delta = -1.216 \pm 0.004$ mas yr^{-1}), distance from isochrone fitting (2.41 ± 0.27 kpc), and mean RV (-26.86 ± 0.15 km s^{-1}). We adopted a Galactocentric distance of $R_{gc} = 8$ kpc and a circular velocity of $V_{\text{rot}} = 220$ km s^{-1} for the Sun (J. Bovy & S. Tremaine 2012; J. Bovy 2015). We simulated the motion of the cluster by integrating its orbit forward for 5 Gyr and backward for 3.71 Gyr, using 1 Myr time steps, incorporating uncertainties in the distance, proper motion, and RV. Figure 16 shows the Z versus R_{GC} motion, and Figure 17 shows the evolution of R_{GC} over time, where Z is the vertical distance and R_{GC} is the Galactocentric distance.

The orbital analysis of Trumpler 19 yielded several important parameters. The birth radius of the cluster is determined to be $R_{\text{birth}} = 7.51 \pm 0.01$ Kpc, with its current Galactocentric distance measured as $R_{\text{GC}} = 10.96 \pm 0.13$ Kpc. The vertical distance during birth is $Z_{\text{birth}} = 141 \pm 5$ pc and the current vertical distance is $Z_{\text{current}} = -36 \pm 4$ pc from the Galactic plane. The orbit analysis yields an apogalactic distance $R_{\text{apo}} = 11.10 \pm 0.08$ Kpc and a perigalactic distance $R_{\text{peri}} = 6.65 \pm 0.17$ kpc, corresponding to an orbital eccentricity of $e = 0.253 \pm 0.016$. The maximum vertical displacement from the Galactic plane is $Z_{\text{max}} = 301 \pm 40$ pc, and the orbital period is estimated to be $P_{\text{orb}} = 188 \pm 3$ Myr. The space velocity components of the cluster are calculated to be $(U, V, W) = (-9.78 \pm 0.56, -32.09 \pm 0.17, -13.94 \pm 0.95)$ km s^{-1}. To account for the motion relative to the local standard of rest (LSR), we applied corrections using the solar motion values from B. Coşkunoğlu et al. (2011), given by $(U, V, W)_\odot = (8.83 \pm 0.24, 14.19 \pm 0.34, 6.57 \pm 0.21)$ km s^{-1}. After this correction, the LSR-referenced velocity components became $(U, V, W)_{\text{LSR}} = (-0.95 \pm 0.61, -17.90 \pm 0.38, -7.37 \pm 0.97)$ km s^{-1}, yielding a total LSR space velocity of $S_{LSR} = 19.38 \pm 1.21$ km s^{-1}.

The orbital characteristics of Trumpler 19 reveal a history of significant dynamical evolution. Its eccentric, wide-ranging orbit suggests radial migration, likely driven by interactions with the Galactic bar and spiral arms, moving it from its birth location (J. A. Sellwood & J. J. Binney 2002). The elevated vertical displacement of the cluster indicates substantial vertical heating from repeated disk passages and interactions with Galactic structures, making it vulnerable to tidal forces, especially close to perigalacticon (C. G. Lacey 1984). This vulnerability is supported by the extreme mass loss, indicating advanced tidal dissolution (H. J. G. L. M. Lamers et al. 2005a; M. Gieles et al. 2006). The resulting orbit in the $Z \times R_{\text{GC}}$ plane remains broadly consistent in shape under both the axisymmetric and nonaxisymmetric models, though there is a noticeable shift in the present-day position. This indicates that while nonaxisymmetric features may not drastically alter the overall orbital path over Gyr timescales, they can affect local orbital phases. This supports the interpretation of the dynamic history of Trumpler 19. The cluster, once more massive, is now being eroded by external tidal forces and internal dynamical processes like evaporation and relaxation.

7.4. Tidal Filling and Dynamical Vulnerability

The Jacobi radius of a star cluster is the distance from the cluster center where the gravitational influence of the cluster balances with the gravitational pull of a larger external body, such as the host galaxy (A. Ernst et al. 2010). Beyond this
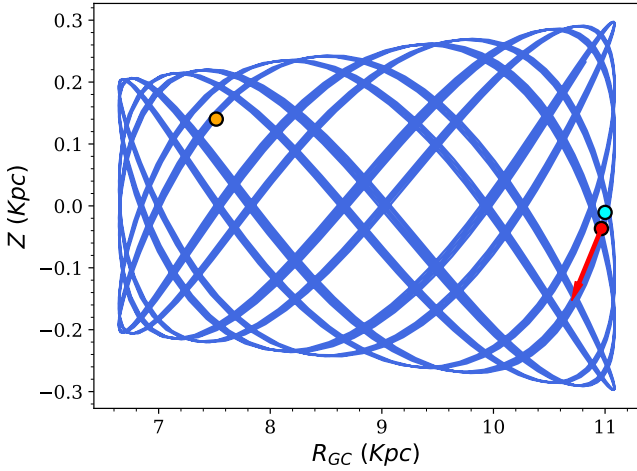
Figure 16. The Galactic orbit of Trumpler 19 in the $Z \times R_{GC}$ plane. The red filled circle marks the present-day location, while the orange filled circle indicates the birth position of Trumpler 19. The red arrow represents the direction of motion within the Galactic potential. The cyan filled circle represents the present-day location only for the MWPotential2014 model.
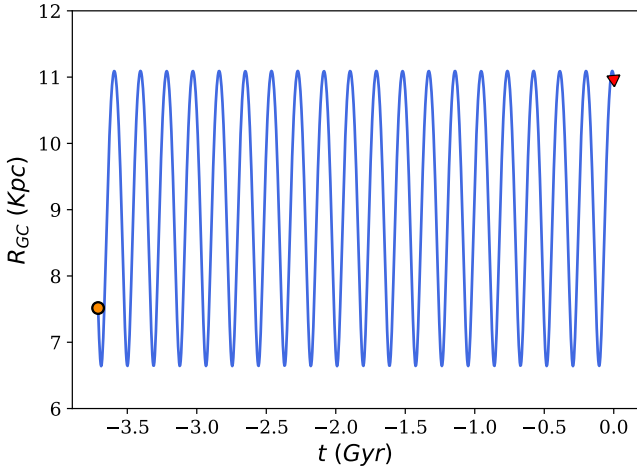

Figure 17. The Galactic orbit and birth radius of Trumpler 19 in the $R_{GC} \times t$ plane. The orange filled circle marks the birth location, while the red filled triangle indicates the present-day position of Trumpler 19.

radius, stars are more likely to become unbound from the cluster, due to the dominant gravitational influence of the galaxy. The Jacobi radius is determined from the equation (S. von Hoerner 1957)

$$r_J = \left(\frac{M_{\text{cluster}}}{3 M_G}\right)^{1/3} R_{GC}, \qquad (28)$$

where M_{cluster} is the cluster mass and M_G is the Milky Way mass inside the Galactocentric distance R_{GC} of the cluster. The value of $M_G = 5 \times 10^{11} M_\odot$ is obtained from the Milky Way mass profile of C. Taylor et al. (2016). The current R_{GC} is obtained as 10.96 Kpc for Trumpler 19. We calculate the Jacobi radius as $18\overset{'}{.}81 \pm 0\overset{'}{.}39$ (12.96 ± 0.29 pc). For Trumpler 19, $r_t > r_J$, which indicates that the cluster is likely to have undergone significant mass-loss processes, potentially moving toward a state of eventual disruption (M. S. Angelo et al. 2018). When the tidal radius exceeds the Jacobi radius, this suggests that external tidal forces from the galaxy are strong

enough to affect stars at distances beyond the Jacobi radius, leading to the stripping of stars and mass from the cluster.

For Trumpler 19, the tidal filling factor, the ratio of the half-mass radius to the tidal radius, $r_h/r_t \sim 0.15$, indicates that the cluster is relatively compact compared to its tidal radius. This suggests that it occupies only a small fraction of its tidal volume, implying that it may be more vulnerable to external tidal forces. While clusters at larger R_{GC} like Trumpler 19 at 10.39 Kpc typically show higher r_h/r_t, due to weaker tidal fields, this nonetheless allows clusters to expand and fill more of their tidal volume without significant disruption (M. S. Angelo et al. 2021). But this observed low r_h/r_t value may indicate past mass loss, possibly from interactions with the Galactic tidal field. Additionally, its eccentric orbit subjects it to varying tidal forces, with stronger tidal effects at perigalacticon, further contributing to mass loss.

To estimate the half-light radius of the cluster, we modeled its radial surface brightness profile using the fluxes of cluster members in the G band from Gaia DR3. It is modeled by measuring the spatial distribution of the stellar flux as a function of the radial distance from the cluster center. The field is divided into concentric annuli centered on the cluster center, and the total G-band flux within each bin is calculated to estimate the surface brightness. Error propagation is performed using the quadrature sum of the individual flux uncertainties. To interpret the observed surface brightness profile, we fitted a point-spread function (PSF)–convolved (I. King 1962) model to the observed light distribution (A. Jordán et al. 2005; D. E. McLaughlin & R. P. van der Marel 2005). The PSF-convolved King model is obtained by convolving Equation (10):

$$I(r) = \rho(r) \otimes \mathcal{G}(r, \sigma), \qquad (29)$$

where $\mathcal{G}(r, \sigma)$ is a Gaussian kernel of width σ. The normalized radial surface brightness profile of the cluster is shown in Figure 18. The black points represent the observed G-band flux distribution, with the error bars indicating the propagated uncertainties. The blue curve shows the best-fit PSF-convolved King model. The PSF-convolved King model is then integrated radially to obtain the cumulative flux profile:

$$F(r) = 2\pi \int_0^r I(r') \, r' \, dr'. \qquad (30)$$

From this resulting cumulative flux profile $F(r)$, we determine the half-light radius r_l, defined as the radius at which the cumulative flux reaches 50% of its total value. Using this method, we calculate the half-light radius, r_l, of Trumpler 19 to be $6\overset{'}{.}74 \pm 0\overset{'}{.}41$ (4.73 ± 0.29 pc). The radial cumulative flux profile based on the I. King (1962) surface density model is shown in Figure 19. The blue curve represents the normalized cumulative flux integrated from the center of the cluster outward.

The tidal filling ratio, the ratio of the half-light radius to its Jacobi radius, r_l/r_J, serves as an important measure of how fully the cluster occupies the gravitational volume permitted by the Galactic tidal field. A higher value of this ratio indicates that the main body of the cluster extends close to its tidal boundary, making it increasingly vulnerable to external tidal influences (A. Ernst & A. Just 2013). This tidal filling factor also correlates with the fraction of stars that escape from the cluster over each relaxation time. Studies by H. M. Lee (2002)
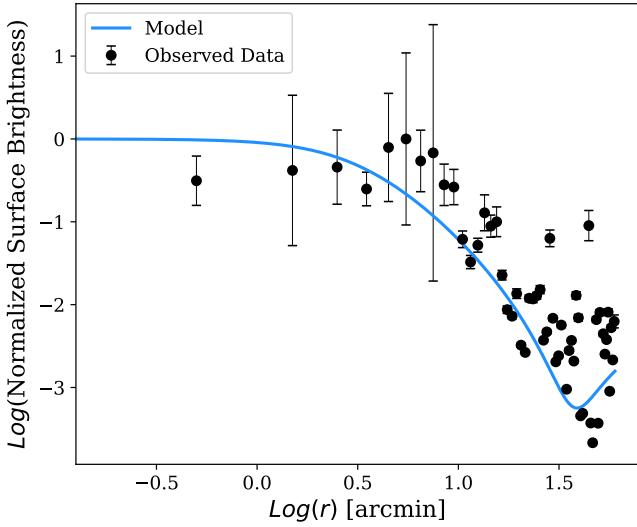
Figure 18. The normalized radial surface brightness profile of the cluster.
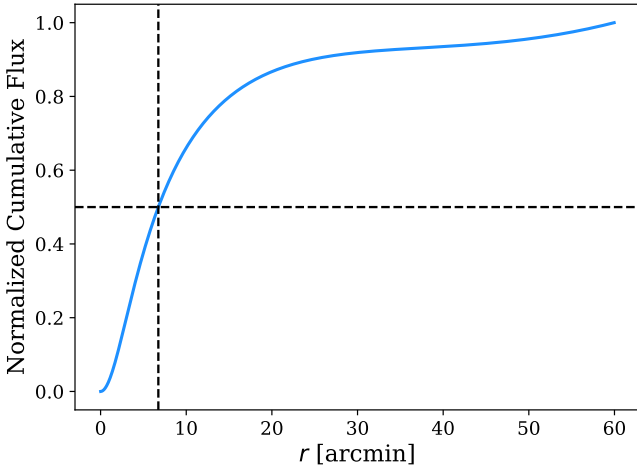

Figure 19. The radial cumulative flux profile based on a PSF-convolved I. King (1962) surface density model.

and M. Gieles & H. Baumgardt (2008) have shown that the evaporation fraction ($\ln\xi$) scales proportionally with r_l/r_J. This relationship arises from the increasing number of stars reaching or exceeding the escape velocity as the cluster becomes more tidally filled. Such a scaling holds true for clusters within the so-called "tidal regime," defined by $r_l/r_J > 0.05$ (H. M. Lee 2002; M. Gieles & H. Baumgardt 2008). Within this regime, the interplay between internal dynamics and external tidal forces becomes a dominant factor in the long-term evolution and stability of the cluster.

For Trumpler 19, we find that $r_l/r_J = 0.37$, for its current R_{GC} of 10.96 Kpc, which places it well within the tidal regime, where external tidal forces from the Galaxy have a significant influence on the dynamical evolution. This indicates that the cluster nearly fills its Roche volume, suggesting that it is highly susceptible to tidal stripping. In such a configuration, a substantial number of stars reside near the tidal boundary and are thus more easily removed by the Galactic gravitational field. The evolution of the ratio r_l/r_J across its orbit, as shown in Figure 20, with a half-orbit timescale of 94 Myr, indicates that the cluster is periodically overfilling its tidal radius near the perigalacticon, where it likely experiences strong tidal
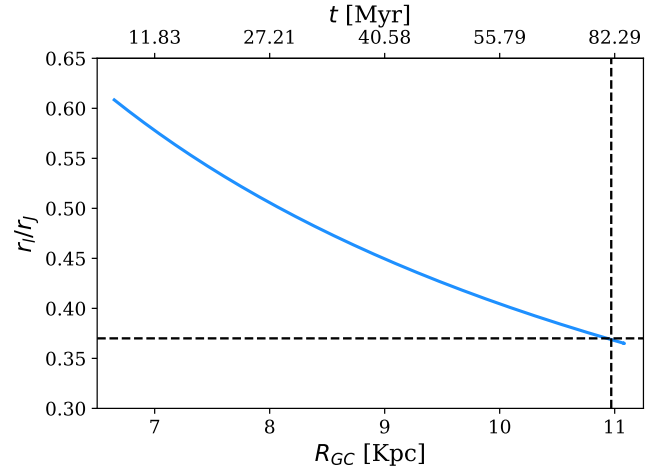
Figure 20. The evolution of r_l/r_J for Trumpler 19 across its orbit, showing periodic tidal overfilling near perigalacticon due to its eccentric orbit.

shocks and subsequent mass loss. Notably, the internal relaxation time of the cluster is about 96 Myr, which is almost the same as its half-orbit time of 94 Myr. This means the cluster does not have enough time to fully adjust to this periodically changing tidal force, leading to repeated tidal shocks. As a result, it loses stars more easily and evolves more quickly toward dissolution.

7.5. Mass Loss and Initial Mass

To estimate the total mass lost by Trumpler 19 throughout its evolution and to infer its initial mass, we used the analytical method proposed by H. J. G. L. M. Lamers et al. (2005a). This approach accounts for mass loss due to both stellar evolution and external tidal influences (H. J. G. L. M. Lamers et al. 2005b). A key advantage of this method is its simplicity, as it relies on analytical formulations derived from extensive N-body simulations to model the time-dependent decrease in cluster mass. The initial cluster mass, M_{ini}, is determined using the following expression:

$$M_{ini} = \left[\left(\frac{M_c}{M_\odot} \right)^\gamma + \gamma \frac{t}{t_0} \right]^{1/\gamma} \cdot [1 - q_{ev}(t)]^{-1}, \quad (31)$$

where M_c represents the current mass of the cluster, t is the cluster age, and t_0 is the characteristic dissolution timescale, which reflects the mass loss due to environmental interactions, such as the Galactic tidal field, encounters with GMCs, and passages through spiral arms (M. Gieles et al. 2006). The exponent γ describes the rate of mass loss and depends on the initial density profile of the cluster. The function $q_{ev}(t)$ quantifies the fractional mass loss attributed to stellar evolution and is a function of time and metallicity. For clusters older than 12.5 Myr, $q_{ev}(t)$ can be approximated by

$$\text{Log}_{10}.q_{ev}(t) = (\text{Log}_{10}.t - a)^b + c, \quad (32)$$

where the constants a, b, and c depend on the metallicity. For Trumpler 19, which has [Fe/H] ≈ -0.05, we adopt the values $a = 7.00$, $b = 0.255$, and $c = -1.805$ from H. J. G. L. M. Lamers et al. (2005a). In our calculations, we used $\gamma = 0.62$, a value commonly found in simulations of open clusters. We also adopt a dissolution timescale $t_0 = 3.3^{+1.4}_{-1.0}$ Myr, which is appropriate for clusters in the solar neighborhood (E. Dalessandro et al. 2015).
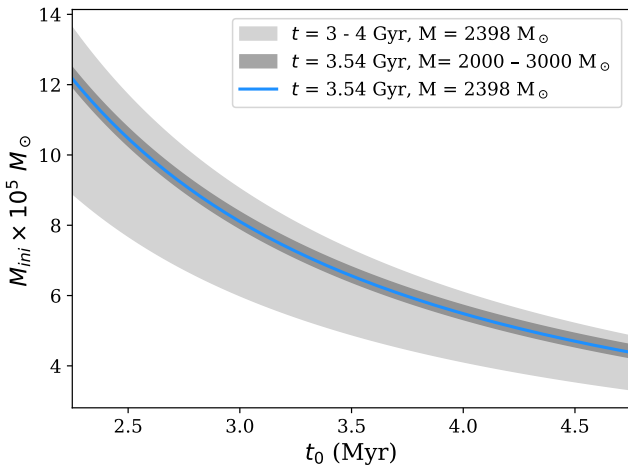
Figure 21. Initial cluster mass as a function of the dissolution timescale parameter t_0. The blue curve represents the relationship considering the current cluster mass of 2398 $M_\odot$ and an age of 3.71 Gyr. The dark gray region illustrates the range of initial masses obtained for current masses between 2000 and 3000 $M_\odot$ at a fixed age of 3.71 Gyr, while the light gray region shows the variation resulting from an age range of 3–4 Gyr for the fixed current mass of 2398 $M_\odot$.

With the current cluster mass of $M_c = 2398\,M_\odot$ and an estimated age of $t = 3.71$ Gyr, we calculate the initial mass for Trumpler 19. The uncertainty in the initial mass estimate arises primarily from the variation in t_0. Figure 21 illustrates how the initial mass depends on t_0 across its uncertainty range, along with the impacts of errors in current mass (considered between 2000 and 3000 $M_\odot$) and age (ranging from 3 to 4 Gyr). The resulting initial mass for Trumpler 19 is found to be $M_{\rm ini} = (6.66 \pm 0.49) \times 10^5\,M_\odot$. This indicates that the cluster has lost over 95% of its original mass since its formation.

8. Results and Discussion

The results obtained from this analysis are discussed as follows:

(i) Using an unsupervised ensemble machine learning approach (S. Deb et al. 2022) on Gaia DR3 astrometric data, we identified 810 cluster members in Trumpler 19 with membership probability >0.54 within a $60'$ search radius. In comparison, X. Gao & D. Fang (2023) identified 859 members, and E. L. Hunt & S. Reffert (2023) identified 896 members within $60'$ for Trumpler 19. We identified 18 BSSs in Trumpler 19, considering an equal-mass binary locus, as shown in Figure 6. X. Gao & D. Fang (2023) identified 24 BSSs without accounting for the equal-mass binary locus.

(ii) From isochrone fitting using a Bayesian MCMC approach, based on Gaia DR3 data, we estimated the astrophysical parameters for Trumpler 19 as follows: distance $\approx 2.37 \pm 0.03$ Kpc, age $\approx 3.71 \pm 0.29$ Gyr, metallicity [Fe/H] $\approx -0.05 \pm 0.12$, extinction $A_v \approx 0.77 \pm 0.07$ mag, and a binary fraction ~ 0.66. Within error, these results align well with those of T. Cantat-Gaudin & F. Anders (2020) and X. Gao & D. Fang (2023).

(iii) Using MCMC analysis, we fitted the radial surface density profile of Trumpler 19 with an I. King (1962) model, estimating a central density $\rho_0 \sim 4.211 \pm 0.193$ stars arcmin^{-2}, core radius $r_c \sim 3.251 \pm 0.127$, tidal radius $r_t \sim 38.85 \pm 1.156$, and background density $\rho_{bg} \sim 0.002 \pm 0.000$ stars arcmin^{-2}. A concentration

parameter $\log(r_t/r_c) \sim 1$ indicates a core–halo structure due to dynamical evolution, and a dynamical evolution parameter $\tau \gg 1$ suggests that Trumpler 19 is dynamically relaxed, suggesting mass segregation within the cluster, including among the BSSs. These results within error are well consistent with those of X. Gao & D. Fang (2023).

(iv) We estimated the slope of the MF for stars with mass $M > 0.4\,M_\odot$. The MF slopes for both single stars and accounting for binary stars are found to be flatter than the E. E. Salpeter (1955) IMF value, indicating a deficiency of low-mass stars, suggesting that the cluster has undergone significant dynamical evolution. The dynamical evolution parameter is found to be $\tau \gg 1$ for Trumpler 19. This also indicates that Trumpler 19 is dynamically relaxed. This is supported by moderate core contraction ($r_c/r_h = 0.54$), consistent with dynamical evolution from two-body relaxation and mass segregation, though core collapse has not yet occurred.

(v) We estimated the fractional mass excess (M_e) of the identified BSSs from ZAMS to understand their formation mechanisms. We found that binary mass transfer and mergers are the prominent formation mechanisms in Trumpler 19. To support this, we searched for the TESS LCs for these 18 BSSs, of which six BSSs showed signatures of variability. We found that these BSSs showed the characteristics of an eclipsing binary (β Persei (Algol) or β Lyrae type), with an orbital period ranging from 0.12 to 0.47 days. The short orbital periods of these eclipsing binary systems suggest that these BSSs may have formed through the mass transfer channel.

(vi) We studied the mass segregation among BSSs using RCDF. We found that BSSs are more concentrated toward the center than the reference MSTO stars, with a statistical significance of 99.99%. This strongly supports the presence of mass segregation in the cluster, particularly among the BSSs. Now, to characterize the mass segregation among the cluster members as well as BSSs, we used the MST method. We found moderate signatures of mass segregation present in Trumpler 19. To study the dynamical state and determine the sedimentation level of the BSSs, we used the A_{rh}^+ parameter. We found A_{rh}^+ to be 0.28 ± 0.05 for Trumpler 19. This also indicates a moderate level of BSS concentration toward the cluster center.

(vii) Trumpler 19 exhibits clear signs of advanced dynamical evolution and tidal disruption. With a tidal radius exceeding its Jacobi radius and a tidal filling ratio of $r_l/r_J \sim 0.37$, the cluster lies well within the tidal regime, i.e., it nearly fills its Roche volume, indicating significant mass loss and susceptibility to tidal stripping. The cluster experiences periodic tidal overfilling near perigalacticon on a ~ 94 Myr half-orbit timescale, comparable to its internal relaxation time ~ 96 Myr, resulting in recurrent tidal shocks. A low tidal filling factor, $r_h/r_t \sim 0.15$, suggests a compact structure, likely shaped by extensive historical mass loss, estimated to exceed 95% of its initial mass $\sim 6.66 \times 10^5\,M_\odot$. Its eccentric, wide-ranging orbit, affected by radial migration and vertical heating from disk crossings, further supports this scenario.

Therefore, the observed mass segregation, particularly among BSSs, along with a flatter MF slope, indicate prolonged

internal dynamical processing. The high binary fraction and BSS variability with a very short period point to active mass transfer and merger events. The radial distribution further confirms the central concentration of massive stars. Externally, the cluster shows the strong influence of Galactic tidal forces, suggesting substantial mass loss and that it is nearing dissolution. Its dynamical state reflects a complex interplay of internal relaxation and external tidal stripping, shaped by orbital migration, marking Trumpler 19 as a dynamically evolved, tidally affected open cluster.

ORCID iDs

A. H. Sheikh ⓘ https://orcid.org/0009-0009-0399-0381
Biman J. Medhi ⓘ https://orcid.org/0000-0002-3448-8150
Ram Sagar ⓘ https://orcid.org/0000-0003-4973-4745

References

Agarwal, M., Rao, K. K., Vaidya, K., & Bhattacharya, S. 2021, MNRAS, 502, 2582
Alessandrini, E., Lanzoni, B., Ferraro, F. R., Miocchi, P., & Vesperini, E. 2016, ApJ, 833, 252
Allison, R. J., Goodwin, S. P., Parker, R. J., et al. 2009, MNRAS, 395, 1449
Almeida, A., Monteiro, H., & Dias, W. S. 2023, MNRAS, 525, 2315
Anders, P., & Fritze-v. Alvensleben, U. 2003, A&A, 401, 1063
Angelo, M. S., Corradi, W. J. B., Santos, J. F. C. J., Maia, F. F. S., & Ferreira, F. A. 2021, MNRAS, 500, 4338
Angelo, M. S., Piatti, A. E., Dias, W. S., & Maia, F. F. S. 2018, MNRAS, 477, 3600
Angelo, M. S., Santos, J. F. C. J., Maia, F. F. S., & Corradi, W. J. B. 2023, MNRAS, 522, 956
Baumgardt, H., & Makino, J. 2003, MNRAS, 340, 227
Bianchini, P., van de Ven, G., Norris, M. A., Schinnerer, E., & Varri, A. L. 2016, MNRAS, 458, 3644
Biswas, S., Medhi, B. J., Deb, S., et al. 2024, MNRAS, 532, 1241
Bovy, J. 2015, ApJS, 216, 29
Bovy, J., & Tremaine, S. 2012, ApJ, 756, 89
Breger, M., Stich, J., Garrido, R., et al. 1993, A&A, 271, 482
Cantat-Gaudin, T., & Anders, F. 2020, A&A, 633, A99
Carrera, R., Pasquato, M., Vallenari, A., et al. 2019, A&A, 627, A119
Chabrier, G. 2003, PASP, 115, 763
Chatterjee, S., Rasio, F. A., Sills, A., & Glebbeek, E. 2013, ApJ, 777, 106
Choi, J., Dotter, A., Conroy, C., et al. 2016, ApJ, 823, 102
Coşkunoğlu, B., Ak, S., Bilir, S., et al. 2011, MNRAS, 412, 1237
Cover, T., & Hart, P. 1967, ITIT, 13, 21
Cox, D. P., & Gómez, G. C. 2002, ApJS, 142, 261
Dalessandro, E., Miocchi, P., Carraro, G., Jílková, L., & Moitinho, A. 2015, MNRAS, 449, 1811
de La Fuente Marcos, R. 1997, A&A, 322, 764
Deb, S., Baruah, A., & Kumar, S. 2022, MNRAS, 515, 4685
Dehnen, W. 2000, AJ, 119, 800
Deisenroth, M. P., Faisal, A. A., & Ong, C. S. 2020, Mathematics for Machine Learning (Cambridge: Cambridge Univ. Press)
Dias, W. S., Monteiro, H., Moitinho, A., et al. 2021, MNRAS, 504, 356
Dib, S., & Henning, T. 2019, A&A, 629, A135
Efron, B., & Tibshirani, R. 1993, An Introduction to the Bootstrap (London: Macmillan)
Elson, R., Hut, P., & Inagaki, S. 1987, ARA&A, 25, 565
Ernst, A., & Just, A. 2013, MNRAS, 429, 2953
Ernst, A., Just, A., Berczik, P., & Petrov, M. I. 2010, A&A, 524, A62
Foreman-Mackey, D., Hogg, D. W., Lang, D., & Goodman, J. 2013, PASP, 125, 306
Gaia Collaboration, Prusti, T., de Bruijne, J. H. J., et al. 2016, A&A, 595, A1
Gaia Collaboration, Vallenari, A., Brown, A. G. A., et al. 2023, A&A, 674, A1
Gao, X., & Fang, D. 2023, Ap&SS, 368, 73
Gao, X.-h. 2019, MNRAS, 486, 5405
Gieles, M., & Baumgardt, H. 2008, MNRAS, 389, L28
Gieles, M., Portegies Zwart, S. F., Baumgardt, H., et al. 2006, MNRAS, 371, 793
Guszejnov, D., Markey, C., Offner, S. S. R., et al. 2022, MNRAS, 515, 167
Hunt, E. L., & Reffert, S. 2023, A&A, 673, A114
Jadhav, V. V., & Subramaniam, A. 2021, MNRAS, 507, 1699
Jordán, A., Côté, P., Blakeslee, J. P., et al. 2005, ApJ, 634, 1002
Khalisi, E., Amaro-Seoane, P., & Spurzem, R. 2007, MNRAS, 374, 703
Kharchenko, N. V., Piskunov, A. E., Schilbach, E., Röser, S., & Scholz, R. D. 2013, A&A, 558, A53
King, I. 1962, AJ, 67, 471
Kroupa, P. 2001, MNRAS, 322, 231
Lacey, C. G. 1984, MNRAS, 208, 687
Lamers, H. J. G. L. M., Baumgardt, H., & Gieles, M. 2010, MNRAS, 409, 305
Lamers, H. J. G. L. M., Gieles, M., Bastian, N., et al. 2005a, A&A, 441, 117
Lamers, H. J. G. L. M., Gieles, M., & Portegies Zwart, S. F. 2005b, A&A, 429, 173
Lanzoni, B., Ferraro, F. R., Alessandrini, E., et al. 2016, ApJL, 833, L29
Lee, H. M. 2002, in IAU Symp. 207, Extragalactic Star Clusters, ed. D. P. Geisler, E. K. Grebel, & D. Minniti (San Francisco, CA: ASP), 584
Leigh, N., Sills, A., & Knigge, C. 2011, MNRAS, 416, 1410
Lightkurve Collaboration, Cardoso, J. V. d. M., Hedges, C., et al., 2018 Lightkurve: Kepler and TESS Time Series Analysis in Python, Astrophysics Source Code Library, ascl:1812.013
Lindegren, L., Klioner, S. A., Hernández, J., et al. 2021, A&A, 649, A2
Mahalanobis, P. 1936, Proc. Natl. Inst. Sci. India, 12, 49
Mahalanobis, P. C. 1927, J. Proc. Asiatic Soc. Bengal, 23, 301
Maurya, J., Joshi, Y. C., Samal, M. R., Rawat, V., & Gour, A. S. 2023, JApA, 44, 71
McCrea, W. H. 1964, MNRAS, 128, 147
McLachlan, G. J., & Peel, D. 2000, Finite Mixture Models (New York: Wiley)
McLaughlin, D. E., & van der Marel, R. P. 2005, ApJS, 161, 304
Meylan, G., & Heggie, D. C. 1997, A&ARv, 8, 1
Miyamoto, M., & Nagai, R. 1975, PASJ, 27, 533
Morton, T. D., 2015 isochrones: Stellar Model Grid Package, Astrophysics Source Code Library, ascl:1503.010
Navarro, J. F., Frenk, C. S., & White, S. D. M. 1996, ApJ, 462, 563
Offner, S. S. R., Moe, M., Kratter, K. M., et al. 2023, in ASP Conf. Ser. 534, Protostars and Planets VII, ed. S. Inutsuka, Y. Aikawa, T. Muto, K. Tomida, & M. Tamura (San Francisco, CA: ASP), 275, https://www.aspbooks.org/a/volumes/article_details/?paper_id=40752
Peterson, C. J., & King, I. R. 1975, AJ, 80, 427
Perets, H. B., & Fabrycky, D. C. 2009, ApJ, 697, 1048
Powell, B. P., Kruse, E., Montet, B. T., et al. 2022, RNAAS, 6, 111
Press, W. H., & Rybicki, G. B. 1989, ApJ, 338, 277
Press, W. H., Teukolsky, S. A., Vetterling, W. T., & Flannery, B. P. 2007, Numerical Recipes : The Art of Scientific Computing (Cambridge: Cambridge Univ. Press), https://numerical.recipes/book.html
Prim, R. C. 1957, BSTJ, 36, 1389
Rain, M. J., Ahumada, J. A., & Carraro, G. 2021, A&A, 650, A67
Rain, M. J., Carraro, G., Ahumada, J. A., et al. 2020, AJ, 159, 59

Rao, K. K., Vaidya, K., Agarwal, M., Balan, S., & Bhattacharya, S. 2023, MNRAS, 526, 1057

Rao, K. K., Vaidya, K., Agarwal, M., & Bhattacharya, S. 2021, MNRAS, 508, 4919

Sagar, R., & Richtler, T. 1991, A&A, 250, 324

Salpeter, E. E. 1955, ApJ, 121, 161

Sandage, A. R. 1953, AJ, 58, 61

Schulz, J., Fritze-v. Alvensleben, U., Möller, C. S., & Fricke, K. J. 2002, A&A, 392, 1

Sellwood, J. A., & Binney, J. J. 2002, MNRAS, 336, 785

Sheikh, A. H., Deka, S., & Medhi, B. J. 2025, MNRAS, 536, 174

Sheikh, A. H., & Medhi, B. J. 2024a, MNRAS, 534, 4031

Sheikh, A. H., & Medhi, B. J. 2024b, AJ, 168, 274

Sheikh, A. H., & Medhi, B. J. 2024c, MNRAS, 528, 7037

Spitzer, L. 1987, Dynamical Evolution of Globular Clusters (Princeton, NJ: Princeton Univ. Press)

Spitzer, L. J., & Hart, M. H. 1971, ApJ, 164, 399

Sturges, H. A. 1926, JASA, 21, 65

Sung, H., Bessell, M. S., Chun, M.-Y., et al. 2017, ApJS, 230, 3

Sung, H., Lim, B., Bessell, M. S., et al. 2013, JKAS, 46, 201

Tarricq, Y., Soubiran, C., Casamiquela, L., et al. 2021, A&A, 647, A19

Tarricq, Y., Soubiran, C., Casamiquela, L., et al. 2022, A&A, 659, A59

Taylor, C., Boylan-Kolchin, M., Torrey, P., Vogelsberger, M., & Hernquist, L. 2016, MNRAS, 461, 3483

Terlevich, E. 1987, MNRAS, 224, 193

Tremmel, M., Fragos, T., Lehmer, B. D., et al. 2013, ApJ, 766, 19

Vesperini, E. 2010, RSPTA, 368, 829

von Hoerner, S. 1957, ApJ, 125, 451